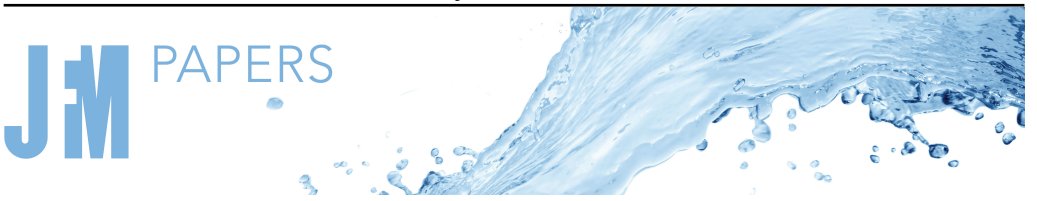
J. Fluid Mech. (2026), *vol.* 1038, A1, doi:10.1017/jfm.2026.11593



Droplet impact dynamics on micropillar-structured surfaces with heterogeneous wettability

Geng Wang[1,2,3], **Jianlong Ren**[1,3], **Xiao Zhao**[1,2], **Ziyi Guo**[1], **Linlin Fei**[4], **Kai Li**[1,3] **and Kai Hong Luo**[5]

[1]National Microgravity Laboratory, Institute of Mechanics, Chinese Academy of Sciences, Beijing 100190, PR China

[2]National Key Laboratory of Spacecraft Thermal Control, Beijing Institute of Spacecraft System Engineering, China Academy of Space Technology, Beijing 100094, PR China

[3]School of Engineering Science, University of Chinese Academy of Sciences, Beijing 100049, PR China

[4]Key Laboratory of Thermo-Fluid Science and Engineering of Ministry of Education, School of Energy and Power Engineering, Xi'an Jiaotong University, Xi'an, Shaanxi 710049, PR China

[5]Department of Mechanical Engineering, University College London, Torrington Place, London WC1E 7JE, UK

Corresponding authors: Kai Hong Luo, k.luo@ucl.ac.uk; Kai Li, likai@imech.ac.cn

(Received 15 July 2025 UTC; revised 7 April 2026 UTC; accepted 10 April 2026 UTC)

Droplet impingement is one of the most common phenomena in nature. However, the impact dynamics of droplets on structured heterogeneous wettability surfaces remain little explored. In this work, an investigation is conducted into the droplet impact on heterogeneous wettability surfaces composed of superhydrophobic micropillars on a hydrophilic substrate, by using an improved phase-field lattice Boltzmann model. In particular, the effects of surface geometry and impact conditions on droplet bouncing and wetting behaviours are scrutinised. Four distinct impact outcomes are identified: complete bouncing, pancake bouncing, partial wetting and complete wetting. Based on the competition among capillary, inertial and viscous forces, an analytical model is proposed to predict the maximum droplet penetration depth within the pillar gaps. A transition diagram is constructed to distinguish these different impact outcomes, with regime boundaries derived from the proposed analytical model. Finally, from the perspective of energy analysis, both the evolution of the energy budget and the surface energy distribution

© The Author(s), 2026. Published by Cambridge University Press. This is an Open Access article, distributed under the terms of the Creative Commons Attribution licence (https://creativecommons.org/licenses/by/4.0/), which permits unrestricted re-use, distribution and reproduction, provided the original article is properly cited.

https://doi.org/10.1017/jfm.2026.11593 Published online by Cambridge University Press

during the droplet impact process are revealed. These findings provide guidance for the design of heterogeneous wettability surfaces, enabling predictable control over droplet bouncing and wetting behaviours.

Key words: drops, capillary flows

1. Introduction

Droplet impact on solid surfaces is one of the most common fluid phenomena in nature, and research into its dynamics can be traced back more than a century (Worthington 1908). Generally, droplet impact dynamics is determined by surface configurations (e.g. surface geometry, wettability) and impact conditions (e.g. fluid properties, impact velocity) (Yarin 2006; Yu *et al.* 2021; Wang *et al.* 2023*c*). Depending on the combination of these parameters, droplets exhibit different impact outcomes, such as adhesion, rebound or splashing (Rioboo, Tropea & Marengo 2001; Josserand & Thoroddsen 2016). Numerous studies have investigated droplet morphologies and dynamic behaviours upon impact with substrates, aiming to achieve precise control over droplet impact outcomes (Liang & Mudawar 2017*a*; Zhao *et al.* 2023). Such fundamental physical understanding provides essential theoretical foundations for industrial and engineering applications, including inkjet printing (Lohse 2021), spray cooling (Liang & Mudawar 2017*b*; Gu *et al.* 2025) and anti-icing (Cao *et al.* 2009).

Typically, the physical properties of a flat surface, such as solid–liquid and solid–gas interfacial tensions, remain homogeneous regardless of surface structure variations (Josyula *et al.* 2024), and the three-phase contact angle is also fixed as described by Young's equation (Young 1805). Depending on the contact angle, these surfaces can be categorised as superhydrophilic, hydrophilic, hydrophobic or superhydrophobic (Yan, Gao & Barthlott 2011). Among these, superhydrophobic surfaces, inspired by natural systems such as the lotus leaf (Barthlott & Neinhuis 1997), have received extensive attention due to their wide-ranging applications in self-cleaning and anti-icing technologies (Rothstein 2010). When a droplet impacts a superhydrophobic surface, a typical evolution process includes spreading, retraction and bouncing. The work of Richard, Clanet & Quéré (2002*a*) demonstrated that the bouncing time of the droplet is independent of impact velocity and follows the Rayleigh limit (Rayleigh 1879). In recent years, numerous superhydrophobic surface designs including column structures (Girard, Soto & Varanasi 2019; Ding *et al.* 2021), ridge structures (Gauthier *et al.* 2015; Guo *et al.* 2018; Hu *et al.* 2022) or curved structures (Liu *et al.* 2015; Shen *et al.* 2017; Abolghasemibizaki, McMasters & Mohammadi 2018) have been proposed to reduce the solid–liquid contact time, the review by Hu *et al.* (2023) has comprehensively summarised recent progress in this field. Among these advances, the study by Liu *et al.* (2014) demonstrated that superhydrophobic micropillar arrays can trigger 'pancake bouncing,' where the droplet lifts off in a pancake-like shape. This effect converts capillary energy stored during penetration into upward kinetic energy (KE) (Moevius *et al.* 2014), thereby reducing the droplet–surface contact time by up to 80 %.

However, droplets impacting homogeneous wettability surfaces usually exhibit a uniform dynamic response, such as wetting and bouncing cannot occur simultaneously for a fixed surface design, regardless of the impact conditions. This limitation means that homogeneous surfaces cannot meet the complex requirements of cutting-edge engineering applications (Li *et al.* 2020*b*; Luo *et al.* 2023). A corresponding solution is to employ heterogeneous wettability surfaces with designed patterns of hydrophobic and hydrophilic

https://doi.org/10.1017/jfm.2026.11593 Published online by Cambridge University Press

regions to meet demanding requirements (Zhu *et al.* 2019; Yang *et al.* 2020). On such surfaces, different areas possess distinct wettabilities, thereby introducing complex solid–liquid interactions that enable precise control over droplet behaviour. A typical example is the Namib desert beetle (*Stenocara*), which collects and transports water for survival in the Namib Desert through a heterogeneous wettability strategy (Parker & Lawrence 2001). This concept has greatly inspired the design and application of heterogeneous wettability in a variety of fields such as optical and electronic device fabrication (Leng *et al.* 2018; Abe *et al.* 2020), cellular interactions (Li *et al.* 2015; Leite *et al.* 2017; Feng, Ueda & Levkin 2018) and biosensing (Huang *et al.* 2013; Li *et al.* 2020*a*). Nevertheless, most existing studies on droplet impact on homogeneous wettability surfaces focus on applications and fabrication techniques (Li *et al.* 2020*b*), with relatively few addressing the impact dynamics or developing surface design criteria for determining droplet bouncing behaviours from a fluid mechanics perspective.

In recent years, droplet dynamics on structured surfaces have received extensive research attention (Wang, Wu & Nestler 2023*a*; Wang *et al.* 2023*c*), particularly on micropillar-structured surfaces, which are considered a typical design for achieving superhydrophobicity (Quéré 2002; Yoshimitsu *et al.* 2002). One key issue in the research of droplet dynamics on pillar-structured surfaces is determining the critical conditions for the transition between the Wenzel state and the Cassie state (Lafuma & Quéré 2003; Reyssat & Quéré 2009). For example, both Deng *et al.* (2009) and Chen *et al.* (2011) suggested that, for impacting droplets, the criterion for achieving either the Wenzel state or the Cassie state is determined by balancing hammer pressure, dynamic pressure and capillary pressure. Murakami, Jinnai & Takahara (2014) developed an energy barrier model describing the energy landscape from the Cassie state to the Wenzel state, demonstrating that the transition is primarily dictated by the competition between the energy barrier and the Laplace pressure. On the other hand, some recent studies have reported droplet dynamics on surfaces with composite wettability, such as superhydrophobic dots (Lenz & Lipowsky 1998; Majhy, Singh & Sen 2020), stripes (Bliznyuk *et al.* 2009; Jansen *et al.* 2012; Wang *et al.* 2019; Wu *et al.* 2019) or patterns (Kusumaatmaja & Yeomans 2007; Wu *et al.* 2020, 2022) on hydrophilic substrates. However, these surfaces are mostly two-dimensional in design, and the research focus has been on droplet wetting behaviours (Wang *et al.* 2023*a*). Studies on the droplet impact dynamics on three-dimensional micropillar-structured surfaces with heterogeneous wettability remain absent.

Usually, fabricating three-dimensional heterogeneous wettability surfaces is complex and costly (Li *et al.* 2020*b*; Luo *et al.* 2023). In particular, variations in the geometry and wettability contrast of microstructures can have a significant influence on droplet impact outcomes, which poses challenges for experiments. As an alternative, numerical simulations offer 'controlled numerical experiments', in which all geometric, physical and operating parameters can be specified precisely and easily while the complete dynamic process, in addition to the impact outcomes, can be studied under various conditions. Especially in studies of droplet dynamics on micropillar surfaces, numerical simulations can provide the opportunity to observe highly transient interfacial evolution within micropillar gaps at the microscale and to obtain quantitative data such as velocity distributions (Xia *et al.* 2024). In recent years, the lattice Boltzmann method (LBM) has emerged as a powerful and efficient computational fluid dynamics tool, particularly well suited for simulating multiphase flows with complex boundary geometries due to its inherent collision–streaming mechanism (Li *et al.* 2016; Hosseini & Karlin 2023). However, conventional multiphase LBM models are limited in their accessible parameter ranges, such as density and viscosity ratios (Aidun & Clausen 2010). In response, many recent studies have focused on proposing advanced collision operators (Mazloomi,

https://doi.org/10.1017/jfm.2026.11593 Published online by Cambridge University Press

Chikatamarla & Karlin 2015; Bösch, Dorschner & Karlin 2018; Fei, Luo & Li 2018) and multiphase models (Li, Luo & Li 2012; Geier, Fakhari & Lee 2015; Wöhrwag *et al.* 2018) to extend the boundary of simulation parameters. To facilitate flexible switching between different collision operators and to enable the extension of advanced models across various collision schemes, Luo, Fei & Wang (2021) have proposed a unified lattice Boltzmann (ULBM). Within this framework, multiphase flow models can be constructed according to specific simulation requirements, allowing for an optimal balance between computational efficiency and capability (Wang, Fei & Luo 2022; Wang *et al.* 2023*b*).

In recent years, the LBM has been employed to simulate droplet impact on striped surfaces with heterogeneous wettability, enabling systematic studies of droplet splitting and spreading dynamics (Lee *et al.* 2017; He *et al.* 2024). However, current research on droplet impact dynamics on heterogeneous wettability surfaces remains insufficient to meet the broad range of application requirements. In particular, in biomedical fields, there is an urgent need to design surfaces that enable selective bouncing or wetting of droplets under different impact conditions for applications such as cell screening (Chen & Zhang 2020; Li *et al.* 2020*b*). To this end, we propose a heterogeneous wettability surface design composed of superhydrophobic micropillars on a hydrophilic substrate to achieve selective bouncing or wetting of impacting droplets. A force balance analysis of droplet penetration processes within the micropillar array is conducted, and a predictive model for droplet penetration is proposed. Then a systematic LBM simulation of the droplet impingement is performed, we demonstrate that droplets impacting such surfaces can exhibit four distinct outcomes: pancake bouncing, complete bouncing, partial wetting and complete wetting. We establish predictive criteria for the different impact outcomes through a proposed analytical model and perform an energy analysis of the droplet evolution. The paper is organised as follows, § 2 outlines the numerical methods and simulation set-up, § 3 presents the results and discussion, the conclusion is provided in § 4.

2. Numerical methods and set-up

2.1. *Model description*

To simulate the two-phase flow, a non-orthogonal phase-field (PF) model is employed. In the PF model, an improved conservative Allen–Cahn (AC) equation is used for interface tracking (Chiu & Lin 2011), i.e.

$$\frac{\partial \phi}{\partial t} + \nabla \cdot (\phi \boldsymbol{u}) = \nabla \cdot M_\phi \left(\nabla \phi - \frac{\boldsymbol{n}}{w_{in}} \left[1 - \tanh^2 \left(\frac{2T}{W_{in}} \right) \right] \right), \tag{2.1}$$

where ϕ is the phase indicator, for the liquid phase $\phi_l = 1$ and for the gas phase $\phi_g = 0$, with $\phi_0 = (\phi_l + \phi_g)/2 = 0.5$ indicating the position of the interface; $\boldsymbol{n} = \nabla\phi/|\nabla\phi|$ is the unit vector normal to the interface; M_ϕ is the mobility and W_{in} stands for the interface thickness. In this work, unless otherwise specified, W_{in} is set to 5 lattices. Here $\boldsymbol{u} = [u_x,\ u_y,\ u_z]$ is the fluid velocity. A signed-distance function T is introduced to avoid any jumps or discontinuities at the interface (Jain 2022; Liang *et al.* 2023), where

$$T = \frac{W_{in}}{4} \ln \left(\frac{\phi}{1 - \phi} \right). \tag{2.2}$$

For the PF multiphase model, the conservative AC equation is coupled with incompressible Navier–Stokes (NS) equations, where the fluid flow is described as (Unverdi & Tryggvason 1992)

https://doi.org/10.1017/jfm.2026.11593 Published online by Cambridge University Press

$$\nabla \cdot \boldsymbol{u} = 0,$$
$$\frac{\partial (\rho \boldsymbol{u})}{\partial t} + \nabla \cdot (\rho \boldsymbol{u}\boldsymbol{u}) = -\nabla P + \nabla \cdot \left(\rho \nu \left(\nabla \boldsymbol{u} + \nabla \boldsymbol{u}^T \right) + \rho \left(\nu_b - \frac{2}{3}\nu \right) (\nabla \cdot \boldsymbol{u}) \boldsymbol{I} \right) + \boldsymbol{F_s} + \boldsymbol{F_b}, \tag{2.3}$$

with ρ the fluid density, ν the fluid kinematic viscosity, ν_b represents the non-hydrodynamic bulk viscosity and P is the pressure; $\boldsymbol{F_s}$, $\boldsymbol{F_b}$ are the surface tension and external body force, respectively:

$$\begin{aligned} \boldsymbol{F_s} &= \mu_\phi \nabla \phi, \\ \boldsymbol{F_b} &= \boldsymbol{g} \rho. \end{aligned} \tag{2.4}$$

Here $\boldsymbol{g}$ is gravity and $\mu_\phi = 4\beta(\phi - \phi_l)(\phi - \phi_g)(\phi - \phi_0) - k\nabla^2\phi$ is the chemical potential, the surface tension γ is related to the parameters $\beta = 12\gamma/w_{in}$ and $k = 3\gamma w_{in}/2$.

In this study, the ULBM is adopted to solve the above governing equations, where the collision equation for the multiple relaxation time (MRT) ULBM model can be expressed as (Luo *et al.* 2021)

$$f_i(\boldsymbol{x} + \boldsymbol{e}_i \Delta t, t + \Delta t) = f_i^*(\boldsymbol{x}, t) = \boldsymbol{M}^{-1}(\boldsymbol{I} - \boldsymbol{S})\boldsymbol{M} f_i(\boldsymbol{x}, t) + \boldsymbol{M}^{-1}\boldsymbol{S}\boldsymbol{M} f_i^{eq}(\boldsymbol{x}, t) + \Delta t \boldsymbol{M}^{-1}\left(\boldsymbol{I} - \frac{\boldsymbol{S}}{2}\right)\boldsymbol{M}C_i, \tag{2.5}$$

where f_i and f_i^* are the pre-collision and post-collision distribution functions, respectively, f_i^{eq} is the equilibrium distribution function and C_i is the external forcing term, $\boldsymbol{e}_i$ and $\Delta t = 1$ are the discrete velocities and the time step, respectively, and $\boldsymbol{I}$ stands for the unit matrix.

To capture the realistic dynamic behaviours of droplets in three dimensions, the D3Q19 discrete velocity model is adopted. Two different distribution functions are introduced to solve the conservation AC equation and the incompressible NS equations:

$$\begin{aligned} \boldsymbol{m}_\phi^* &= \left(\boldsymbol{I} - \boldsymbol{S}_\phi\right)\boldsymbol{m}_\phi + \boldsymbol{S}_\phi \boldsymbol{m}_\phi^{\boldsymbol{eq}} + \Delta t \left(\boldsymbol{I} - \frac{\boldsymbol{S}_\phi}{2}\right)\boldsymbol{R}_\phi, \\ \boldsymbol{m}_g^* &= \left(\boldsymbol{I} - \boldsymbol{S}_g\right)\boldsymbol{m}_g + \boldsymbol{S}_g \boldsymbol{m}_g^{eq} + \Delta t \left(\boldsymbol{I} - \frac{\boldsymbol{S}_g}{2}\right)\boldsymbol{R}_g. \end{aligned} \tag{2.6}$$

Here $\boldsymbol{m}_\phi = \boldsymbol{M} f_{\phi,i}$ is for the conservation AC equation and $\boldsymbol{m}_g = \boldsymbol{M} g_i$ is for the incompressible NS equations. For the non-orthogonal MRT collision operator, the transformation matrix $\boldsymbol{M}$ is chosen as the simplified non-orthogonal moment set that was originally proposed by Fei *et al.* (2018, 2019). In (2.6) the discrete equilibrium moment sets and the discrete forcing terms such as $\boldsymbol{m}_\phi^{eq} = \boldsymbol{M} f_{\phi,i}^{eq}$, $\boldsymbol{m}_g^{eq} = \boldsymbol{M} g_i^{eq}$, $\boldsymbol{R}_g = \boldsymbol{M} C_{g,i}$ and $\boldsymbol{R}_\phi = \boldsymbol{M} C_{\phi,i}$ are given explicitly in our previous work (Wang *et al.* 2023*b*). After the collision step in raw moment space (2.6), the distribution functions can be reconstructed as $g_i = \boldsymbol{M}^{-1}\boldsymbol{m}_g^*$ and $f_{\phi,i} = \boldsymbol{M}^{-1}\boldsymbol{m}_\phi^*$.

To model the wetting behaviours involved in the following cases, we employed an energy-based contact angle model, in which the relationship between the solid phase indicator (ϕ_s) and the apparent contact angle (θ) can be expressed as (Zarareh *et al.* 2021)

$$\boldsymbol{n} \cdot \nabla \phi_s = -\sqrt{\frac{2\beta}{\kappa}} \phi_s (1 - \phi_s) \cos\theta. \tag{2.7}$$

https://doi.org/10.1017/jfm.2026.11593 Published online by Cambridge University Press

	Density	Dynamic viscosity	Surface tension
Gas phase	$\rho_g = 1.17\ \mathrm{kg\ m^{-3}}$	$\mu_g = 18.45\ \mu\mathrm{Pa \cdot s}$	$\sigma = 0.072\ \mathrm{N\ m^{-1}}$
Liquid phase	$\rho_l = 997.05\ \mathrm{kg\ m^{-3}}$	$\mu_l = 890.08\ \mu\mathrm{Pa \cdot s}$	—

Table 1. Fluid properties in current simulations.

In the following simulations the solid boundaries are implemented as no-slip for the fluid momentum, while the singularity at the moving contact line is regularised by the diffuse-interface PF model (Jacqmin 2000; Yue, Zhou & Feng 2010). In the present study, a static contact angle model is adopted without considering contact angle hysteresis, since our focus is on droplet impingement dynamics rather than on the detailed evolution of the moving contact line. This modelling assumption leads to a significantly simplified treatment and is sufficient for the present purpose, as supported by the comparison between simulations and experiments shown in § 2.2. The effects associated with detailed moving-contact-line physics, which may become important on hydrophilic surfaces or surfaces with significant contact angle hysteresis, will be addressed in future work. The above contact angle model can be used to simulate complex surfaces with a wide range of wettabilities. Detailed validations are provided in Appendix A. The above ULBM PF model was implemented in C++ and parallelised using the message passing interface. It has been integrated into our in-house software suite UCLBM (unified cascaded LBM). We have used this model to simulate a range of complex multiphase flow behaviours, such as phase change multiphase flow in porous media (Yang *et al.* 2024) and droplet breakup in electric fields (Wang *et al.* 2024).

2.2. *Comparison with experiments*

Before simulating the main cases, we first validated the numerical model in the above section. Specifically, we conducted a validation and mesh convergence study by simulating the impingement of a water droplet on a flat superhydrophobic surface and comparing the results with the experiments by Zhang *et al.* (2022). The initial droplet radius was set to $R_0 = 1.05\ \mathrm{mm}$, the impact Weber number $We = \rho_l R_0 V_0^2/\sigma$ was 20 and the superhydrophobic surface had a contact angle of $\theta_0 = 165°$. The liquid phase is water and the gas phase is air, with their properties listed in table 1. The simulation domain is set as a rectangular box of size $L_x \times L_y \times L_z = 300 \times 300 \times 600$. Considering the symmetric nature of the problem, planar symmetry boundary conditions are imposed at $L_x = 0$ and $L_y = 0$. Figure 1(*a*) presents the time evolution of the spreading radius for different grid resolutions, the results demonstrate that the grid is sufficiently fine when $\mathrm{d}x \leq R_0/45$, and the mesh size has negligible influence on the final results. During the evolution, the average relative error between the simulation and the experiment is about 8 %, with the maximum error occurring at the point of maximum spreading diameter. This may be attributed to the absence of contact angle hysteresis effects in our simulation. Figure 1(*b*) presents qualitative comparison snapshots of our simulation results (left, blue) and the experimental results (right, black). It can be seen that our simulation accurately captures the droplet dynamics, including the splitting of a satellite droplet at $t = 9.1\ \mathrm{ms}$.

To validate the accuracy of the adopted ULBM (PF) model in capturing droplet dynamics on microstructured surfaces, a comparative study was conducted between simulation results and experimental data (Liu *et al.* 2014). We first reproduced the experiment of a water droplet impacting a pillared superhydrophobic surface at two different Weber numbers, $We = 4.7$ and $We = 7.9$, using the same pillar geometry as in the

https://doi.org/10.1017/jfm.2026.11593 Published online by Cambridge University Press

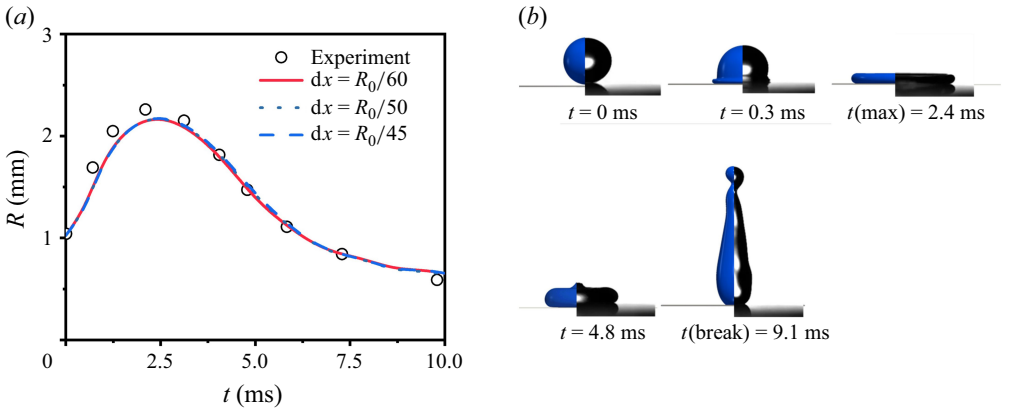


Figure 1. Comparison between simulation and experimental results for a water droplet impacting a flat superhydrophobic surface at $We = 20$: (*a*) time evolution of the droplet radius for various mesh sizes; (*b*) comparison of droplet morphology.

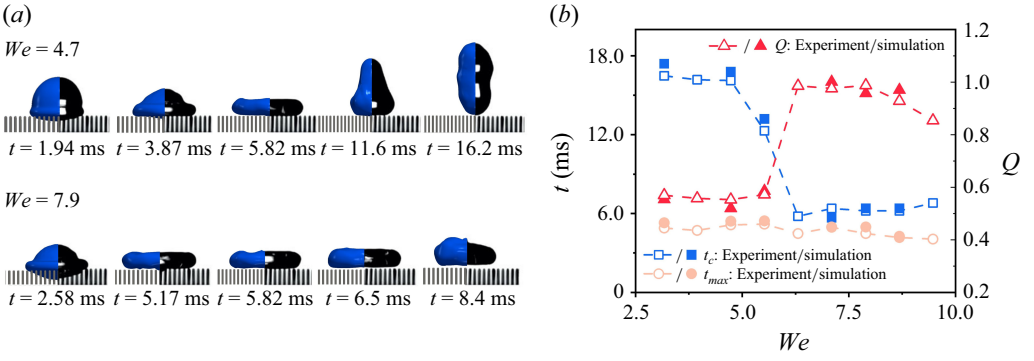


Figure 2. Comparison between simulations and experimental results for a water droplet impacting on a pillared superhydrophobic surface at different *We*. (*a*) Qualitative comparison of droplet bouncing morphologies. (*b*) Quantitative comparison of contact time (t_c), maximum time (t_{max}) and rebound factor (Q).

experimental set-up (Liu *et al.* 2014). In this case, the simulation domain and boundary conditions are identical to those in figure 1. A mesh resolution of $dx = R_0/43$ is employed to match the experimental ratio of droplet radius to micropillar size. Figure 2(*a*) shows the evolution of droplet bouncing morphologies, where the left (blue) side displays the simulation results and the right (black) side presents the experimental snapshots (Liu *et al.* 2014). It can be found that, for the case at $We = 4.7$, the droplet exhibits a typical complete rebound morphology, undergoing spreading, retraction and rebounding after contacting the surface. Consistent with Rayleigh's theory (Richard, Clanet & Quéré 2002*b*; Strutt 2011), the droplet–surface contact time is approximately $t_c/t_\sigma \approx 2.2$, where the inertial capillary time $t_\sigma = \sqrt{\rho_l R_0^3/\sigma}$. For the case at $We = 7.9$, part of the droplet overcomes the capillary resistance between the superhydrophobic micropillars and penetrates into the pillar gaps. In this process, the KE is partially converted into surface energy (SE) and then the penetrated portion is rapidly expelled from the pillar gaps, resulting in a shortened liquid–solid contact time of approximately $t_c/t_\sigma \approx 0.65$. In addition, we have verified that the results for droplet impact on micropillar surfaces are independent of both grid resolution and interface width, details can be found in Appendix B.

https://doi.org/10.1017/jfm.2026.11593 Published online by Cambridge University Press

We then extended our simulations to a wider range of *We* and quantitatively compared the results with experimental data (Liu *et al.* 2014). Three key variables were examined: the contact time t_c, representing the duration of droplet–surface interaction; t_{max}, the time at which the droplet reaches its maximum spreading diameter; and the spreading factor Q, defined as the ratio of the droplet diameter at lift off to its maximum spreading diameter. As shown in figure 2(*b*), our simulated values show strong agreement with experimental measurements across a broad range of *We*. In particular, the model successfully captures the transition from complete rebound to pancake bouncing with increasing *We*. The good agreement in both the qualitative and quantitative evolution of the droplet between simulation and experiment confirms that the proposed model can accurately capture the complex interactions between droplets and structured surfaces.

2.3. *Problem description*

As summarised in the introduction, a knowledge gap still exists regarding the impact dynamics of droplets on heterogeneous wettability surfaces composed of superhydrophobic micropillars on a hydrophilic substrate. Such surface designs introduce complex interactions between the droplet and solid structures with contrasting wettability, resulting in droplet impingement outcomes that depend strongly on both surface geometry and impact conditions. For example, prior studies (Song *et al.* 2017; Tao *et al.* 2022) suggest that droplets can exhibit either pancake bouncing or complete bouncing when impacting on superhydrophobic micropillar surfaces under different *We*. Besides, it has been widely observed that droplets exhibit complete wetting or partial wetting when impacting on hydrophilic surfaces (Rioboo *et al.* 2001; Dawson *et al.* 2023). Building on this knowledge, it can be expected that droplets may exhibit a variety of complex outcomes after impingement, like pancake bouncing, complete rebound and adhesion morphologies, depending on different impact conditions and surface geometries. Therefore, the key research objective of the present study is to reveal the underlying mechanisms of droplet impact on micropillar-structured surfaces with heterogeneous wettability and to identify the critical conditions that determine each bouncing morphology.

Figure 3 illustrates the simulation domain used for the subsequent cases, which has dimensions of length $L_x = 360$, width $L_y = 360$ and height $L_z = 540$, in lattice grid units. Considering that we focus on vertically impacting droplets, only a quarter of the domain is simulated by employing symmetric boundary conditions to improve computational efficiency. As shown in figure 3, the lower boundary is configured as a heterogeneous wettability surface consisting of a hydrophilic substrate with a square array of superhydrophobic micropillars. The hydrophilic substrate has a contact angle $\theta_s = 30°$, whereas the superhydrophobic micropillars have a contact angle $\theta_p = 150°$. A zoomed-in side view of the patterned surface is provided in the dashed box to highlight the micropillar configuration. Here, h_p and s_p denote the pillar height and the centre-to-centre spacing between the pillars, respectively, while w_p represents the width of an individual micropillar. The surface opening fraction, defined as $f = (s_p - w_p)/s_p$, is used to quantify the opening fraction density.

For all subsequent cases, unless otherwise specified, the initial droplet radius is set to $R_0 = 290\,\mu$m, corresponding to 60 lattice grids ($dx = 4.8\,\mu$m) in the simulation domain. Notably, a finer mesh resolution was employed in the simulations of the main cases, enabling the study of micropillar geometries across a broader range of parameters. The micropillar width is fixed at $w_p = R_0/15$, the centre-to-centre spacing s_p varies from $s_p = R_0/12$ to $s_p = R_0/6$, resulting in a surface opening fraction f ranging from 0.2 to 0.6. In line with the validation cases in § 2.2, the liquid phase is water and the gas phase is air,

https://doi.org/10.1017/jfm.2026.11593 Published online by Cambridge University Press

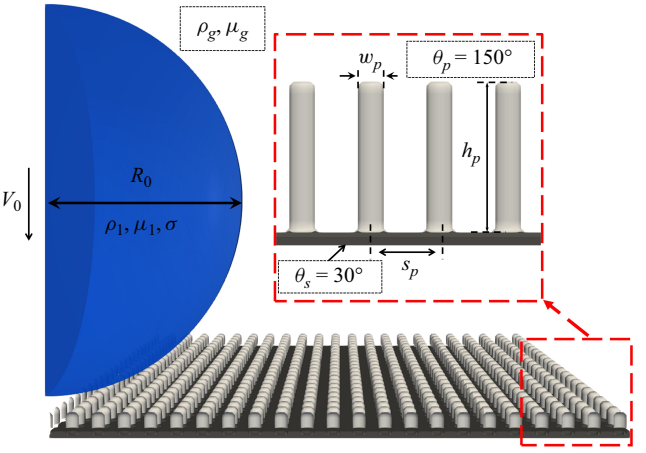


Figure 3. Sketch of the simulation domain, with a zoomed-in view within the red dashed box illustrating the detailed configurations of the mixed-wettability micropillar surfaces.

with their properties listed in table 1. It is worth noting that, thanks to the robustness of the adopted ULBM (PF) model, we are able to achieve realistic water–air density and viscosity ratios in our simulations, which are usually difficult to achieve in traditional LBM multiphase models (Li *et al.* 2016; Mazloomi Moqaddam, Chikatamarla & Karlin 2017). The Weber number (*We*) is used to characterise the effect of impact velocity V_0 and the dimensionless pillar height $H^* = h_p/R_0$ is used to represent the influence of micropillar height.

2.4. *Force balance analysis of droplet impingement*

In this section we present a force balance analysis of the droplet impact and penetration processes. To predict wetting and bouncing behaviours of droplets on the heterogeneous wettability surfaces, it is essential to establish an analytical model that describes the liquid penetration process within the pillars after droplet impact. A key objective is to derive a predictive relation for the maximum penetration depth of the droplet as a function of f and *We*. The penetration of liquid into the pillar gaps is governed by the competition among inertial force, viscous force and capillary force. In our work, the total capillary resistance force ($F_{capillary}$) is modelled as the sum of three contributions: (i) the meniscus pressure difference across the pillar gaps, given by $2\gamma\cos(\theta_p)/(s_p - w_p)$, (ii) the number of meniscus under the contact area, which can be approximated as R_c^2/s_p^2, (iii) the effective meniscus area under the contact region, considering that the meniscus cannot completely wet the pillar gaps during penetration, it can be scaled as $(1 - \lambda f)R_c^2$, thus,

$$F_{capillary} \sim \frac{2\gamma\cos\left(\theta_p\right)}{\left(s_p - w_p\right)} \cdot \frac{R_c^2}{s_p^2} \cdot (1 - \lambda f)\, R_c^2, \tag{2.8}$$

where R_c is the contact radius between the droplet and the tops of the pillars, and the geometry related constant λ is chosen as 1.5 in our model. As shown in previous studies (Riboux & Gordillo 2014; Philippi, Lagrée & Antkowiak 2016), for droplets impacting and penetrating porous surfaces, the time evolution of the contact line follows $R_c/R_0 \sim t^{0.5}$. Assuming that the vertical evolution of the droplet scales as $(R_0 - \Delta h)/R_0 \sim t^{-1}$, we

https://doi.org/10.1017/jfm.2026.11593 Published online by Cambridge University Press

have $((R_0 - \Delta h)/R_0)^{-0.5} \sim R_c/R_0$. Substituting $f = (s_p - w_p)/s_p$ into (2.8) yields

$$F_{capillary} \sim \frac{\gamma \cos\left(\theta_p\right) R_0^4 \left(1 - 1.5f\right)}{s_p^2 \left(R_0 - \Delta h\right)}. \tag{2.9}$$

In addition, the viscous force $F_{viscous}$ during the droplet evolution can be scaled as $F_{viscous} \sim \mu_l \Delta h'/R_0$, related to the reference velocity gradient $\Delta h'$ (Delbos, Lorenceau & Pitois 2010). To facilitate the analysis, we only consider the forces on the symmetry plane of the droplet. In accordance with Newton's second law, we can establish the equation of motion:

$$m^* \frac{\mathrm{d}^2 \Delta h}{\mathrm{d}t^2} = \frac{\gamma \cos\left(\theta_p\right) R_0^4 \left(1 - 1.5f\right)}{s_p^2 \left(R_0 - \Delta h\right)} - \frac{\mu_l}{R_0} \frac{\mathrm{d}\Delta h}{\mathrm{d}t}. \tag{2.10}$$

Here m^* is the effective mass on the two-dimensional plane with a dimension of $kg\ m^{-2}$, scaled as $m^* \sim \rho_l R_0$. Normalising (2.10) using $\Delta h^* = \Delta h/R_0$ and T^*, the equation becomes

$$\frac{\mathrm{d}^2 \Delta h^*}{\mathrm{d}T^{*2}} = \frac{\cos\left(\theta_p\right) R_0^2 \left(1 - 1.5f\right)}{s_p^2 (1 - \Delta h^*)} - Oh \frac{\mathrm{d}\Delta h^*}{\mathrm{d}T^*}, \tag{2.11}$$

where the Ohnesorge number is $Oh = \mu_l/\sqrt{\gamma \rho_l R_0}$. By substituting the initial conditions, i.e. $\Delta h^*(0) = 0$ and $\Delta h^{*\prime}(0) \sim V_0 = \alpha\sqrt{We}$, the transient evolution of Δh^* can be derived. It is noteworthy that in the above governing equation, a fitting parameter $\alpha = 0.56$ is introduced to balance the effects of capillary and viscous forces. This parameter is determined by fitting the analytical model to simulation results for the maximum penetration depth across a range of cases. Its value may vary with different combinations of surface tension and viscosity. All other force terms are derived from realistic forcing balance. Thus, (2.11) can be directly applied to droplets of various sizes and different surface geometries. It should be clarified that the above model is only applicable to the penetration process after droplet impact on micropillar surfaces. For the rebound process, the direction of the viscous force changes, rendering this equation inapplicable. However, considering that the main objective here is to identify the relationship between the maximum droplet penetration depth and the parameters We and f, analysing the penetration process is sufficient.

During droplet impact, when the penetration depth exceeds the pillar height ($\Delta h^*_{max} > H^*$), the droplet exhibits a Wenzel state due to the hydrophilicity of the substrate; otherwise, the droplet remains in the Cassie state ($\Delta h^*_{max} < H^*$). Therefore, Δh^*_{max} can be used as a criterion for determining the bouncing outcomes of the impacting droplet. In the current study the capillary number $Ca = \mu_l V_0/\gamma$, which represents the ratio of viscous force to surface tension, is at least one order of magnitude smaller than 10^{-1}. As a result, the viscous term in (2.11) can be safely neglected. By implementing $V = \Delta h^{*\prime}$, the equation can thus be simplified as

$$V \frac{\mathrm{d}V}{\mathrm{d}h^*} = \frac{\cos\left(\theta_p\right) R_0^2 \left(1 - 1.5f\right)}{s_p^2 (1 - \Delta h^*)}, \tag{2.12}$$

integrating both sides we obtain

$$\int V \mathrm{d}V = \int \frac{\cos\left(\theta_p\right) R_0^2 \left(1 - 1.5f\right)}{s_p^2 (1 - \Delta h^*)} \mathrm{d}h^*, \tag{2.13}$$

https://doi.org/10.1017/jfm.2026.11593 Published online by Cambridge University Press

and applying the initial conditions, we have

$$\frac{1}{2}V^2 = -\frac{\cos\left(\theta_p\right) R_0^2\left(1-1.5f\right)}{s_p^2}\ln\left(1-\Delta h^*\right)+\frac{1}{2}V_0^2, \tag{2.14}$$

considering that Δh^* reaches its maximum value when $V=0$, Δh^*_{max} can be predicted as

$$\Delta h^*_{max} = 1-\exp\left\{\frac{\alpha^2 s_p^2 We}{2R_0^2\cos\left(\theta_p\right)\left(1-1.5f\right)}\right\}. \tag{2.15}$$

Equation (2.15) can be used to determine the droplet impact outcomes under different impact conditions and surface geometries. It should be noted that the proposed model for predicting the maximum penetration depth covers a wide range of operating parameters, including droplet radius, impact velocity and micropillar geometry, and thus, requires extensive validation to demonstrate its reliability. In addition, several quantitative aspects of droplet dynamics remain to be explored, such as the dynamic evolution of the meniscus within micropillar arrays, the wetting state on hydrophilic substrates and the energy evolution of the droplet. It would be challenging and costly for experiments to provide well-resolved quantitative data of the required transient interfacial dynamics. On the other hand, the lattice Boltzmann simulations allow a systematic study of the dynamics process of droplet impact on heterogeneous wettability surfaces while providing quantitative data to validate the proposed model, as will be demonstrated in the following section.

3. Results and discussion

3.1. *Droplet wetting and bouncing behaviours*

Figure 4 illustrates the transient evolution of the droplet after impact at $We = 12$. Four cases were examined to explore the effects of H^* and f. In contrast to the dynamics of droplet impact on homogeneous wettability surfaces, four distinctly different impact outcomes were observed. For the case with the lowest pillar height and largest opening fraction (panel (*a*), $H^* = 0.08$, $f = 0.56$), part of the liquid penetrates the micropillar array and contacts the substrate directly during droplet spreading (as shown in $T^* = t/t_\sigma =$ 0.25 and 0.75). Subsequently, the droplet fully penetrates the pillars and reaches a complete Wenzel state ($T^* = 1.25$ of panel *a*). Due to the hydrophilicity of the substrate, droplet rebound is suppressed and the droplet demonstrates a complete wetting morphology. For the case with a similar pillar height but smaller opening fraction (panel (*b*), $H^* =$ 0.08, $f = 0.33$), a similar liquid penetration and adhesion process is observed (see $T^* =$ 0.75 and 1.25 in panel *b*). Then, due to the droplet rebound, the Wenzel state is disrupted, and the main part of the droplet bounces off the surface. However, a small portion of the droplet remains adhered to the hydrophilic substrate, resulting in a partial wetting morphology.

As indicated in panels (*a*) and (*b*) of figure 4, Wenzel state droplets exhibit wetting morphologies due to the hydrophilicity of the substrate. On the other hand, Cassie state droplets show evolution similar to that observed during impingement on a superhydrophobic pillared surface. For example, for the case with a smaller opening fraction (panel (*c*), $H^* = 0.05$, $f = 0.2$), the penetration of the liquid is suspended due to the increasing capillary resistance, and the droplet rebound follows a typical complete rebound morphology. For the case with the highest pillar height and largest opening fraction (panel (*d*), $H^* = 0.33$, $f = 0.56$), liquid first penetrates into the micropillar gaps and then retracts before it touches the substrate, the droplet presents a typical pancake bouncing morphology as shown in figure 2.

https://doi.org/10.1017/jfm.2026.11593 Published online by Cambridge University Press

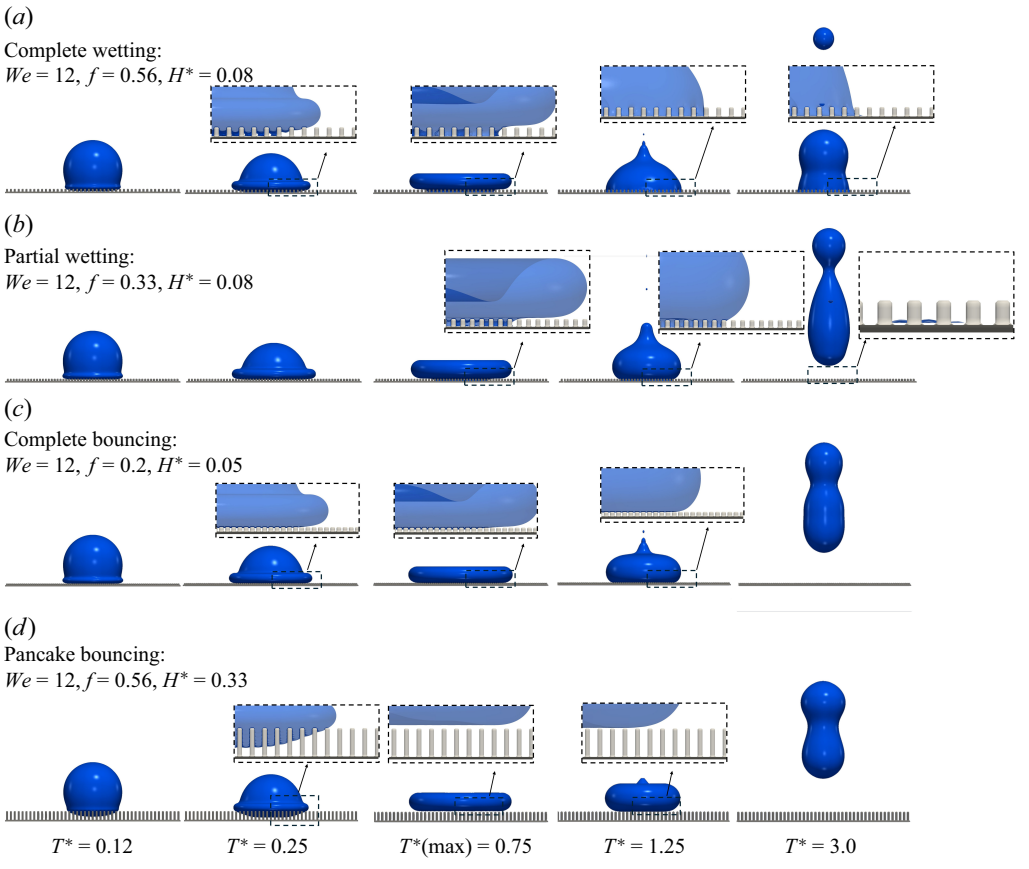


Figure 4. The wetting and bouncing behaviours of droplets impacting mixed-wettability pillared surfaces with varying *We*, pillar height (H^*) and opening fractions (f).

We first focus on the rebound dynamics of droplets in the Cassie state. Figure 5(*a*) depicts the dynamics of a bouncing droplet at varying *We* ($H^* = 0.5$, $f = 0.56$). The droplet is coloured by the normalised pressure ($P/(2\gamma/R_0)$) with velocity vectors (coloured by velocity magnitude) superimposed. At the penetration stage ($T^* = 0.2$), the droplet's bottom penetrates into the pillar gaps, during which the dynamics is governed by the competition between inertial effects and capillary force. For cases with higher *We*, a higher pressure is observed in the penetrated liquid. As anticipated from a previous study (Moevius *et al.* 2014), the KE is converted into SE; therefore, a higher *We* increases the distance between the droplet's bottom surface (P_1) and pillars' top surface (denoted as h in the following). At $T^* = 0.4$, the mother droplet above the pillar surface further spreads while the penetrated liquid begins to retract (as demonstrated by the velocity vector components), during which SE is transferred back to KE. By $T^* = 0.86$, the droplet fully retracts and bounces off from the plate. A higher *We* leads to a larger amount of transferred KE, and therefore, pancake bouncing morphology is clearly observed for the large *We* cases (e.g. $We = 16$). The dynamics of droplet penetration into the pillar gaps is shown in figure 5(*b*) using two-dimensional slices along the symmetry plane. It can be seen that, for all cases in figure 5(*a*), the three-phase contact line moves below the top of the pillars during the penetration stage. Owing to the superhydrophobic wettability of

https://doi.org/10.1017/jfm.2026.11593 Published online by Cambridge University Press

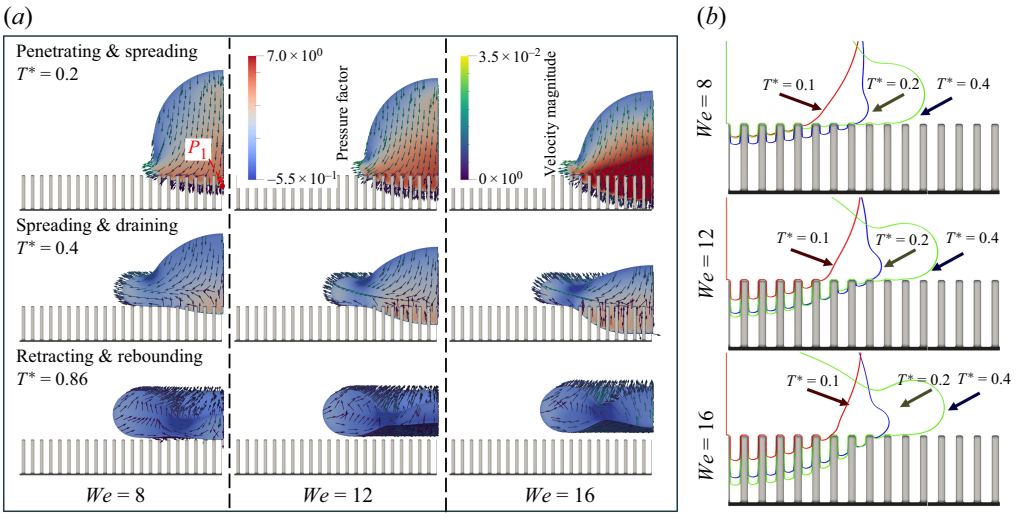


Figure 5. (*a*) The dynamic evolution of droplet impact on mixed-wettability pillared surfaces ($H^* = 0.5$, $f = 0.56$) with varying *We*. (*b*) Two-dimensional slices along the symmetry plane showing the evolution of the droplet profile (highlighted by coloured lines) at $T^* = 0.1$, 0.2 and 0.4 for cases in figure 5(*a*).

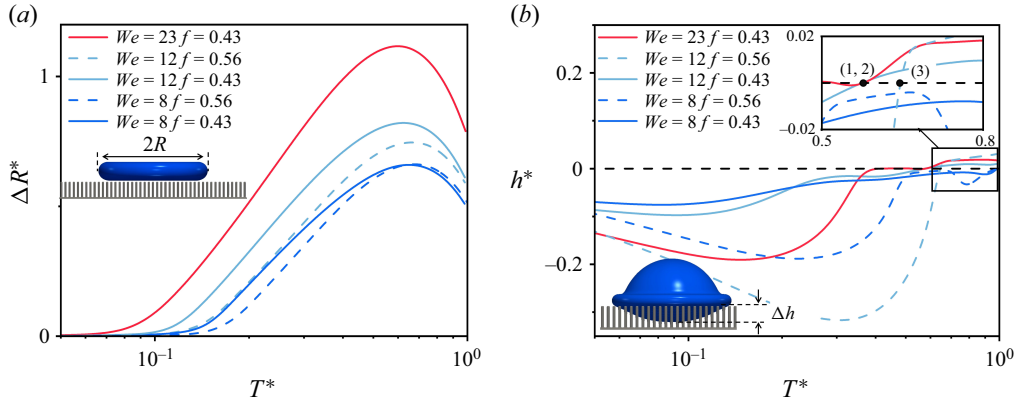


Figure 6. The transient evolution of the normalised (*a*) droplet radius variation (ΔR^*) and (*b*) droplet penetration depth within the pillars (h^*) for cases with varying *We* and opening fractions (f). The inset figure in panel (*b*) illustrates the instant of droplet bouncing off the surface.

the pillar surfaces, the liquid penetrating into the pillar gaps forms curved menisci, which provide one of the main contributions to the capillary resistance force.

To further investigate the influence of micropillar geometry and impact conditions on the transient dynamics of a Cassie state droplet, figure 6 presents the time evolution of the normalised droplet radius variation ($\Delta R^* = (R - R_0)/R_0$, where R denotes the maximum horizontal displacement of the droplet) and penetration depth ($\Delta h^* = (0 - h)/R_0$) for different impact *We* and f. As demonstrated in figure 6(*a*), in all cases, ΔR^* increases initially and then decreases as the droplet retracts. Similar to previous experimental observations for droplet impact on a non-wetting surface (Illias *et al.* 2021; Gao *et al.* 2024), the maximum spreading time is around $t_{max}/t_\sigma \sim 0.8$ and independent of *We*. The maximum spreading diameter of the droplet increases as *We* increases. Figure 6(*b*) shows

https://doi.org/10.1017/jfm.2026.11593 Published online by Cambridge University Press

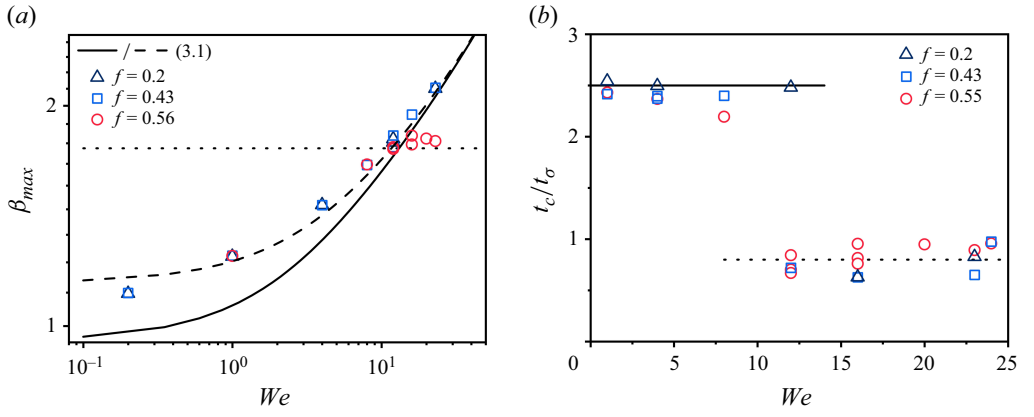


Figure 7. (*a*) Maximum spreading factors (β_{max}) and (*b*) liquid–solid contact time (t_c/t_σ) of droplets impacting mixed-wettability pillared surfaces with varying Weber numbers and opening fractions.

the evolution of h^*, in agreement with the qualitative results shown in figures 4 and 5. Increasing both *We* and f enhances the penetration of the liquid into the pillars, owing to the dominance of dynamic forcing over capillary force in the vertical direction. After reaching the maximum penetration depth, the penetrated liquid drains from the pillar gaps. For the cases with higher *We*, owing to the larger SE storage, the droplet directly rebounds from the plate (points (1, 2, 3) in the inset of figure 6*b*) and exhibits the pancake bouncing morphology with contact time $t_c/t_\sigma < 1$. For the cases with lower *We* (e.g. $We = 8$), the droplet remains in contact with the plate and follows a complete rebound morphology, which is similar to the transient evolution shown in figure 5.

In the following, we focus on the bouncing droplets and quantitatively examine two key parameters during impact: the maximum spreading diameter and the contact time, which are of particular interest for characterising droplet dynamics. In figure 7(*a*) we recorded the droplet maximum spreading diameters and compared our simulation results with the scaling model proposed by Wörner (2023), which can give an accurate prediction of the maximum spreading coefficient β_{max} (ratio of the maximum wetting radius to the initial radius) for a wide range of *We*, where (Wörner 2023)

$$\beta_{max} = \sqrt{\frac{2\left(Q_\beta + a\cos\theta_p\right) + 2\sqrt{\left(Q_\beta + a\cos\theta_p\right)^2 + 4aQ_\beta\left(1-\cos\theta_p\right)}}{1-\cos\theta_p}}, \tag{3.1}$$

where a is a fitting parameter and Q_β is given as

$$\begin{aligned} Q_\beta &= 1 - a + \frac{We}{12} - f_w w_\infty, \\ w_\infty &= 1 - \left(\frac{1}{3}\sqrt{0.25\left(2+\theta_p\right)\left(1-\theta_p\right)^2 + \frac{We}{12}}\right), \\ f_w &= \frac{WeRe^{-2/5}}{1.2 - \cos\theta_p + WeRe^{-2/5}}. \end{aligned} \tag{3.2}$$

The solid line in figure 7(*a*) represents the experimental fitting parameter $a = 0.75$ in Wörner's work (2023) and the dashed line corresponds to $a = 0.6$, providing the best fit to our simulation results. It can be found that, at lower *We* (i.e. $We < 10^1$), the opening fraction f has negligible influence on β_{max} owing to the limited penetrated liquid in the

https://doi.org/10.1017/jfm.2026.11593 Published online by Cambridge University Press

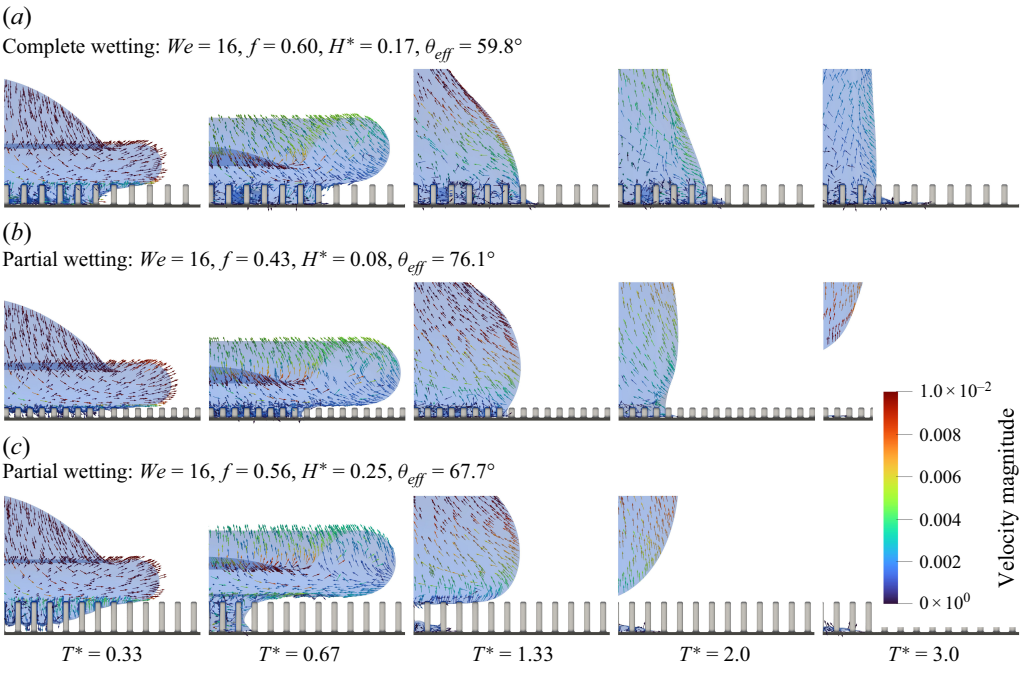


Figure 8. Simulation snapshots (taken along the symmetry plane of the droplet) of droplet impact on surfaces with different micropillar geometries at $We = 16$. Velocity vectors are coloured according to velocity magnitude.

micropillar gaps. At higher We (i.e. $We > 10^1$), for cases with a large f, liquid penetration into the micropillar array results in a nearly constant β_{max} of approximately 1.7. This saturation of the maximum spreading radius due to volume loss through penetration is similar to the observation reported for droplet impacts on superhydrophobic mesh arrays (Kumar *et al.* 2018) and the quantitative results shown in figure 7. For the cases with a smaller f, β_{max} aligns closely with the scaling prediction because of the small amount of liquid penetration in the pillar gaps.

Figure 7(*b*) illustrates t_c/t_σ as a function of We for cases of the Cassie state droplet. It can be seen that the criterion determining the droplet rebound morphology mainly depends on the We. That is, for a lower impact We (i.e. $We < 12$), almost all cases demonstrate complete rebound with $t_c/t_\sigma \approx 2.2$ (solid line in figure 7*b*), consistent with Rayleigh's theory (Ernest, August & Strutt 1879). For higher impact We (i.e. $We > 12$), most cases demonstrate pancake bouncing morphologies with a much shorter $t_c/t_\sigma \approx 0.56$ (dashed line in figure 7*b*), which aligns with previous experimentally measured values. Meanwhile, it can also be observed that a smaller f leads to a higher We for the pancake bouncing regime, as a higher dynamic force is needed to achieve penetration.

We then focus on the wetting dynamics of droplets in the Wenzel state. Figure 8 shows the evolution of wetting droplets for cases with different micropillar geometries at $We = 16$. It can be seen that, for all cases, wetting of the hydrophilic substrate by the penetrated liquid occurs during the impact stage. For the complete wetting droplet (panel *a*), no fragmentation or separation of the main droplet is observed during retraction and rebound stages. Meanwhile, during the retraction stage, the liquid on the substrate retracts more slowly than the mother droplet due to the pinning effect. In contrast, for partially wetted droplets (panels *b* and *c*), either a higher pillar density (smaller s_p)

https://doi.org/10.1017/jfm.2026.11593 Published online by Cambridge University Press

increases the capillary pressure ($\sim 2\gamma \cos(\theta_p)/(s_p - w_p)$) or a greater pillar height (h_p) increases the risk of liquid bridge breakup between the mother droplet and the pinned liquid at the base. As a result, splitting of the pinned liquid from the mother droplet is observed during the retraction stage, and rebound of the mother droplet occurs at the end of the simulation. In this work we introduce an effective contact angle (θ_{eff}) to characterise the competition between pinning (due to the hydrophilic substrate) and depinning (due to the superhydrophobic micropillars) effects. The effective contact angle is constructed using the full form of the Cassie equation (Milne, Amirfazli & Baxter 2012), i.e.

$$\cos\left(\theta_{eff}\right) = \sum_n f_{s,n} \cos\left(\theta_n\right), \tag{3.3}$$

where the summation covers n interfaces under the droplet and $f_{s,n}$ denotes the surface fraction of each component. When the droplet contacts the substrate, the equation reduces to

$$\cos\left(\theta_{eff}\right) = (1 - f_s)\cos\left(\theta_s\right) + f_s \cos\left(\theta_p\right), \tag{3.4}$$

and the solid fraction is given by

$$f_s = \frac{\pi\left((1 - f)\, R_0\right)^2 + 4\,(1 - f)\, R_0 h_p}{\pi R_0^2}. \tag{3.5}$$

It should be noted that (3.4) is only applicable for characterising the Wenzel state. For droplets in the Cassie state, the effective contact angle can be expressed as $\cos(\theta_{eff}) = f_s(\cos(\theta_p) + 1) - 1$. By comparing the qualitative results in figure 8 with θ_{eff} calculated from (3.5), it is found that, as expected, a smaller θ_{eff} promotes pinning, while a larger θ_{eff} facilitates rebound. As a result, the amount of liquid remaining on the surface after rebound is minimised for cases with larger θ_{eff}. It should be noted that we chose R_0 as the reference length scale in (3.5), and the expansion effect of droplets for various *We* has been ignored. Therefore, θ_{eff} is only applicable for evaluating the pinning and depinning effects at a fixed impact *We*.

We now consider the effect of different impact *We* on the dynamics of Wenzel state droplets. Figure 9 illustrates the evolution of the normalised droplet radius ΔR^* (left axis) for both wetting droplets (dashed lines) and bouncing droplets (solid lines). It can be concluded that, for higher *We* (i.e. $We = 12$ and $We = 16$), the terminal droplet radius is larger for complete wetting cases than for rebound droplets, due to the pinning of liquid on the substrate that inhibits retraction (also demonstrated in figure 8). As expected, for lower impact *We*, the suppression of retraction caused by the pinning effect is less pronounced. We also plotted the transient evolution of the liquid–solid contact area ($S^* = S/(\pi R_0^2)$, shown as filled patterns in figure 9*b*) for wetting cases, complemented by qualitative snapshots (figures in dashed brackets) of the bottom surface contact area (blue patterns, coloured by velocity). As shown in the snapshots, a ring-shaped contact area with holes is initially formed, resulting from gas expulsion beneath the spreading film. As the penetrated liquid wets the surface, the contact area increases and reaches its maximum value. Both qualitative and quantitative results indicate that, similar to the case of droplets impacting hydrophilic surfaces, the maximum wetting area for fully wetted droplets also increases with increasing *We* and stabilises during the retraction process.

In conclusion of the above findings, the wetting and bouncing behaviours of droplets on the heterogeneous wettability surfaces are directly governed by the penetration dynamics of liquid into the pillars. In following section, we validate the force balance analysis provided in § 2.4 over a wide range of surface geometrical parameters and impact conditions.

https://doi.org/10.1017/jfm.2026.11593 Published online by Cambridge University Press

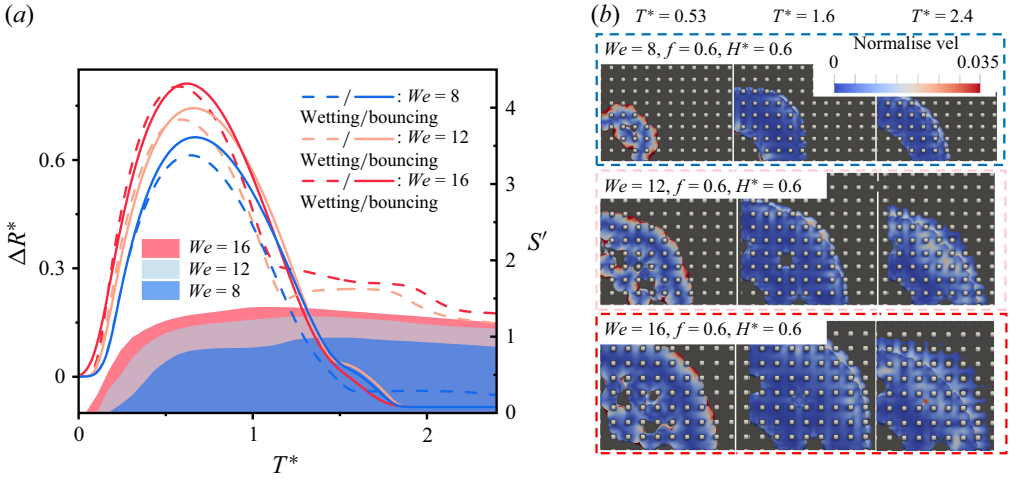


Figure 9. (*a*) The transient evolution of the normalised droplet radius variation (lines in the graph) and liquid–solid contact area (patterns in the graph), (*b*) the qualitative snapshots illustrating the liquid–solid contact area on the bottom surface.

3.2. *Droplet dynamic evolution*

Figures 10(*a*) and 10(*b*) illustrate the evolution of Δh^* for cases with different impact We at $f = 0.56$ (figure 10*a*) and $f = 0.43$ (figure 10*b*), together with a comparison to the proposed model ((2.15), lines in figure). As shown in the figures, our proposed analytical model provides a good prediction of Δh^* during the penetration stage. In addition, it can be observed that Δh^* increases almost linearly (slope = 1.0) with T^* for all cases during the early stage of penetration. This is because the droplet penetration is mainly governed by inertial effects at this stage. At the later stage of penetration, both viscous and capillary forces begin to act and resist further penetration, the penetrated portion eventually retracts after reaching the maximum penetration depth (Δh^*_{max}). As expected, discrepancies between the analytical model and our lattice Boltzmann simulation results begin to emerge during the rebound phase (i.e. time instant after Δh^*_{max}).

Figure 10(*c*) compares the simulated maximum penetration depths (symbols) with the proposed model (line in the figure). It can be seen that our proposed model demonstrates good agreement with the simulation results over a wide range of Δh^*. For most cases, the maximum error is less than 20 % (within the region between the dashed lines). It should be emphasised that the above analytical model is derived based on the competition between forces, and the size effects of both the micropillars and the droplet are taken into account. Therefore, the model is applicable to a wide range of micropillar surface structures, droplet sizes and impact conditions. This generality warrants further validation in future experimental and numerical studies.

Figure 11 presents a transition diagram illustrating the impact outcomes of all cases explored in the current study. The vertical axis shows the criterion of the Cassie state and Wenzel state, which is determined by $\Delta h^*_{max} - H^*$. For the Cassie state droplet with $h^*_{max} - H^* < 0$ and lower We, the droplet undergoes complete rebound due to limited penetration of liquid in the pillars' gap. As We increases, enhanced energy transfer between KE and SE promotes pancake bouncing. A dashed vertical line at $We = 12$ marks the empirical threshold between complete rebound and pancake bouncing, as suggested in previous studies (Liu *et al.* 2014; Wang *et al.* 2025) and supported by our current simulation results. It is worth noting that, near the regime boundary

https://doi.org/10.1017/jfm.2026.11593 Published online by Cambridge University Press

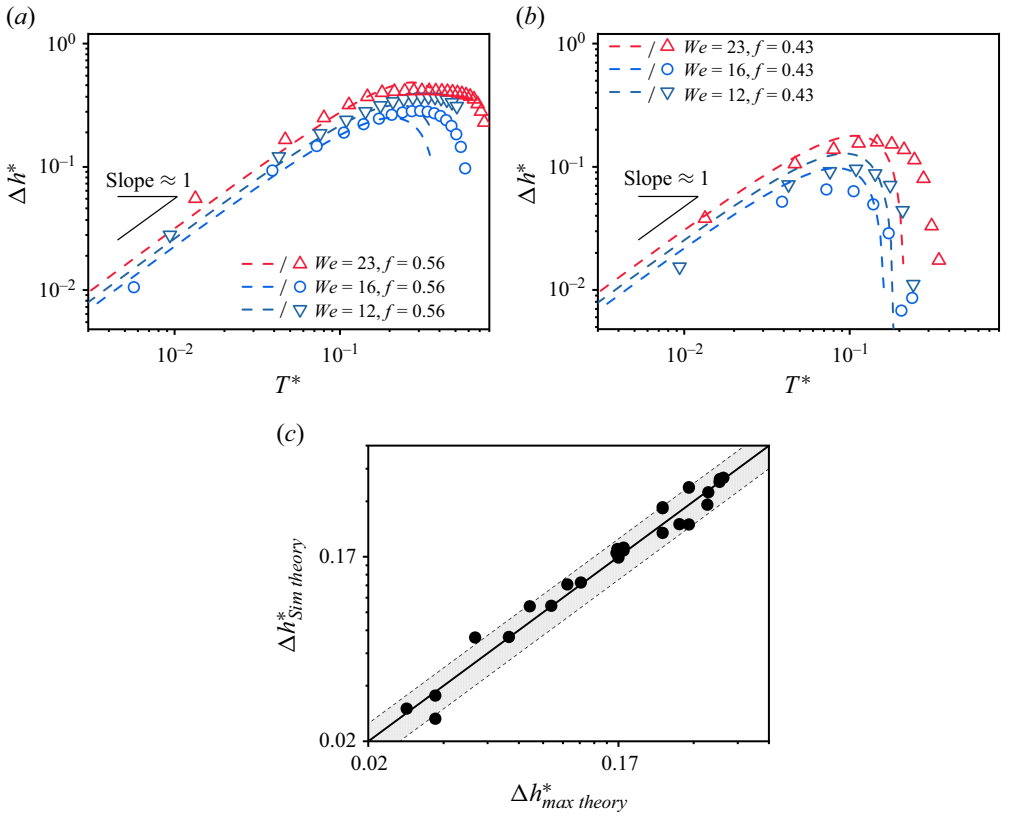


Figure 10. A quantitative comparison of the droplet penetration depth inside pillars under various *We*, with opening fractions of (*a*) $f = 0.56$ and (*b*) $f = 0.43$. Panel (*c*) presents a comparison between the simulation results and the analytical model of the maximum penetration depth, as determined by (2.15).

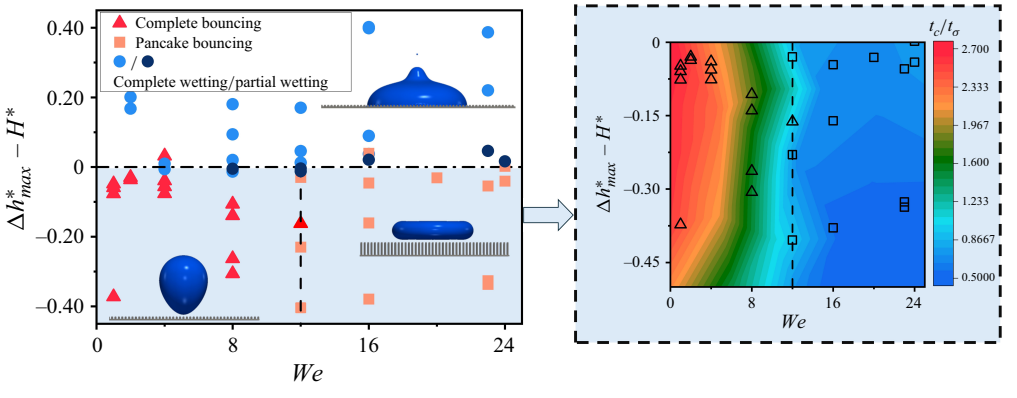


Figure 11. A transition diagram of droplet impact outcomes under varying We, $\Delta h^*_{max} - H^*$ in the vertical axis represents the critical value determined by (2.15).

($We = 12$ and $\Delta h^*_{max} - H^* < 0$), we observed some overlap between pancake bouncing and complete rebound cases. This is because the critical *We* for the onset of pancake bouncing can vary with the micropillar geometry (as shown in figure 7*b*). However, over a broader range of *We* outside the immediate boundary region, using *We* as the

https://doi.org/10.1017/jfm.2026.11593 Published online by Cambridge University Press

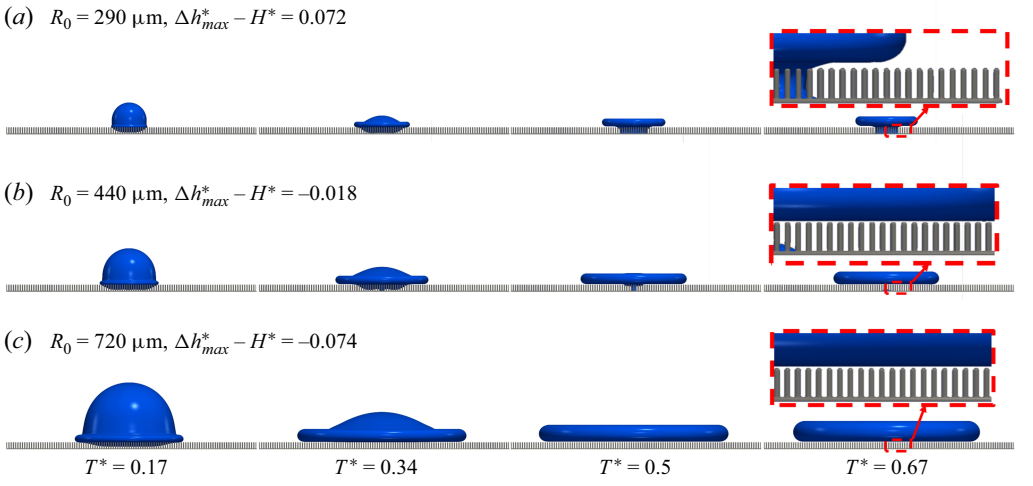


Figure 12. Dynamic evolution of droplet impact on mixed-wettability pillared surfaces ($h_p \approx 106.3\,\mu\text{m}$, $f = 0.56$) with varying R_0.

criterion to distinguish between pancake bouncing and complete rebound remains robust and effective. In addition, we plotted a contour map of t_c/t_σ for all Cassie state droplets in the inset of figure 11 (dashed box). Consistent with the results in figure 7(*b*), as *We* increases, t_c/t_σ decreases due to the occurrence of pancake bouncing. In contrast, the value of $\Delta h^*_{max} - H^*$ has little effect on the rebound time of the droplet.

For cases where $\Delta h^*_{max} - H^* > 0$, the droplet exhibits a Wenzel state with the penetrated liquid wetting the hydrophilic surface. For higher *We*, partial wetting is observed when $\Delta h^*_{max} - H^* \approx 0$. As analysed in figure 8, this is due to the fact that a small penetration depth results in a limited liquid–surface contact area. In such cases, the pinning effect at the hydrophilic substrate is insufficient to overcome the inertia of the rebounding droplet, leading to separation between the mother droplet and the pinned liquid. When $\Delta h^*_{max} - H^* \gg 0$, the increased contact area strengthens the pinning effect and complete wetting is consistently observed. It should be noted that when $\Delta h^*_{max} - H^*$ approaches zero, there are some overlap cases between the Wenzel state and Cassie state. This is attributed to the non-negligible thickness of the gas–liquid interface in our adopted model. However, away from the regime boundary, our current model can robustly predict the outcomes of droplet impact. These results provide important physical insight for interfacial design, especially considering that our model and transition diagram have been validated over a wide range of surface geometries and impact conditions.

To validate the scalability of our proposed model, we further investigate the size effect on droplet impingement. Figure 12 presents the evolution of droplets during impact for different droplet sizes. For all cases in figure 12, the droplet impact conditions are set as $We = 24$, $f = 0.56$ and $h_p \approx 106.3\,\mu\text{m}$. It can be observed that as the droplet radius increases, the penetration depth decreases. This can be attributed to the fact that a larger droplet radius results in a greater contact radius on the pillar surface, which in turn leads to an increased capillary force acting to overcome the droplet's inertia. This effect has been incorporated into our expression for capillary force (2.8).

Furthermore, we extended the tests shown in figure 12 to a broader range of droplet sizes and impact conditions. As shown in figure 13, it is evident that the proposed criterion equation accurately describes the impact outcomes for droplets of different radius. It should be noted that the derivation of the penetration distance in (2.10) neglects the

https://doi.org/10.1017/jfm.2026.11593 Published online by Cambridge University Press

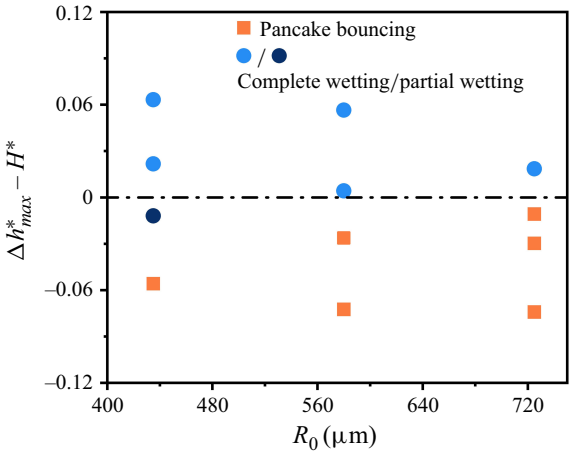


Figure 13. A transition diagram of droplet impact outcomes under varying R_0.

influence of gravity. As a result, the proposed analytical model may become invalid for droplets with a very large radius, where gravitational effects cannot be ignored. Nevertheless, for the typical droplet size range encountered in this work, our model can accurately predict the bouncing or wetting behaviour of droplets under different impact conditions and surface geometries.

3.3. *Droplet energy evolutions*

As discussed in § 3.1, the droplet impact process involves not only the competition among different forces, but also the interconversion between SE, viscous dissipation and KE. Owing to the flexibility of numerical simulations, we are able to obtain quantitative information that is difficult to access experimentally, such as velocity distributions and surface area evolution, enabling detailed energy analysis during droplet impact, which is crucial for understanding the dynamic evolution of the droplet. During the evolution of the droplet, its KE can be expressed as

$$KE = \int \frac{1}{2}\rho \left(u_x^2 + u_y^2 + u_z^2\right) \mathrm{d}\Omega, \tag{3.6}$$

where Ω represents the volume of the liquid phase. When a droplet impacts a surface with hybrid wettability, its SE can be expressed as

$$SE = \gamma_{lg} S_{lg} + \gamma_{sl,b} \cdot S_{sl.b} + \gamma_{sl,p} \cdot S_{sl,p} + \gamma_{sg,b} \cdot S_{sg,b} + \gamma_{sg,p} \cdot S_{sg,p}, \tag{3.7}$$

where γ denotes interfacial tension and S denotes interfacial area. The subscripts lg, sl and sg refer to the liquid–gas, liquid–solid and solid–gas interfaces, respectively. The subscript b indicates the hydrophilic substrate, while p stands for the superhydrophobic micropillar surface. According to the area conservation relations $\Delta S_{sg,p} = -\Delta S_{sl,p}$ and $\Delta S_{sg,b} = -\Delta S_{sl,b}$, (3.7) can be simplified as

$$SE = \gamma_{lg} S_{lg} + \left(\gamma_{sl,b} - \gamma_{sg,b}\right) S_{sl,b} + \left(\gamma_{sl,p} - \gamma_{sg,p}\right) S_{sl,p} + \gamma_{sg,b}\, S_b^{tot} + \gamma_{sg,p}\, S_p^{tot}, \tag{3.8}$$

where $S_b^{tot} = S_{sl,b} + S_{sg,b}$ and $S_p^{tot} = S_{sl,p} + S_{sg,p}$ denote the total substrate and micropillar surface areas, respectively. By applying Young's equation, $\gamma_{sl} = \gamma_{sg} - \gamma_{lg}\cos\theta$ and the relation $\gamma_{sg,b} = \gamma_{sg,p} \approx 0$ as implied by our contact angle model (Zararei *et al.* 2021), the

https://doi.org/10.1017/jfm.2026.11593 Published online by Cambridge University Press

SE expression can be further simplified as

$$SE = \gamma_{lg} S_{lg} - \gamma_{lg} \left(\cos\left(\theta_b\right) S_{sl,b} + \cos\left(\theta_p\right) S_{sl,p}\right). \tag{3.9}$$

During the droplet evolution, the viscous dissipation rate (VDR, Θ) at each fluid element is related to the local viscosity and the velocity gradients. According to the incompressible NS equations recovered from the LBM formulation (2.3), where

$$\Theta = \rho\nu \left(\boldsymbol{\nabla u} + \boldsymbol{\nabla u}^T\right) : \boldsymbol{\nabla u} + \rho \left(\nu_b - \left(\frac{2}{3}\right)\nu\right) (\boldsymbol{\nabla} \cdot \boldsymbol{u})^2 , \tag{3.10}$$

the viscous dissipation energy (VE) during the droplet evolution can be expressed as

$$VE = \int_0^t \int_0^{\Lambda} \Theta \mathrm{d}\Lambda \mathrm{d}t, \tag{3.11}$$

where Λ stand for the whole simulation domain including gas phase and liquid–gas interface. It should be noted that our calculations of KE, SE and VE are based on physical definitions. As a result, achieving accurate energy conservation imposes very strict requirements on the conservation properties of the adopted LBM model. During the evolution of the droplet, the total energy (TE) is given by

$$TE = VE + SE + KE. \tag{3.12}$$

We first evaluated the energy evolution of droplets impacting the same surface ($f = 0.6$, $H^* = 0.17$) at different We, with all energy components normalised by the TE at the initial moment. Theoretically, TE* should remain unity throughout the droplet evolution. As shown in figure 14, for all cases, the dimensionless TE remains close to 1, with a maximum deviation of about 5 %. These small discrepancies may result from statistical errors in measuring the contact area on the micropillars and the substrate. It can be observed that, for the small We case (i.e. $We = 4$), the energy conversion is mainly between KE and SE, with viscous dissipation less than 15 %. As We increases, the proportion of viscous dissipation increases rapidly, reaching up to about 50 % for $We = 12$. The evolution of the VDR in figure 14(*d*) clearly illustrates the mechanism behind the increase in VE: for droplets with higher impact We, VDR is significantly larger during the impact and spreading stages. Interestingly, a double-peak feature is observed in VDR curves, with the second peak corresponding to the retraction and rebound stage. For droplets with smaller We, VDR during this stage can even exceed that of the initial impact stage. This result is in good agreement with recent studies (Hu, Chu & Wu 2022*b*; Zhang *et al.* 2022) reporting a double-peak feature in the impact force of droplets, with the timing ($\approx 1.22 t_\sigma$) of the second peak matching experimental observations. In comparison, the bouncing and wetting morphology of the droplet does not significantly affect the evolution of SE. For example, the terminal SE after droplet retraction for both the complete bouncing droplet ($We = 4$) and complete wetting droplets ($We = 8$ and $We = 12$) returns to levels similar to the initial state. However, for fully wetting droplets, a slight increase in SE is observed after retraction, which can be attributed to the wetting effect of the hydrophilic substrate.

We now consider the energy evolution for different micropillar geometries at $We = 16$, using the effective contact angle (θ_{eff}) to characterise the influence of pillar geometry. It should be noted that, as We increases, the error in the time integration of VE (3.11) may be amplified due to the limited data sampling interval, potentially leading to an underestimation of viscous dissipation during the impact and retraction processes. Consequently, the error in TE also increases. For cases in figure 15, the maximum error in TE is approximately 15 %, which could be reduced in future work by employing denser data sampling. Quantitatively, as θ_{eff} increases, the terminal KE of the droplet decreases

https://doi.org/10.1017/jfm.2026.11593 Published online by Cambridge University Press

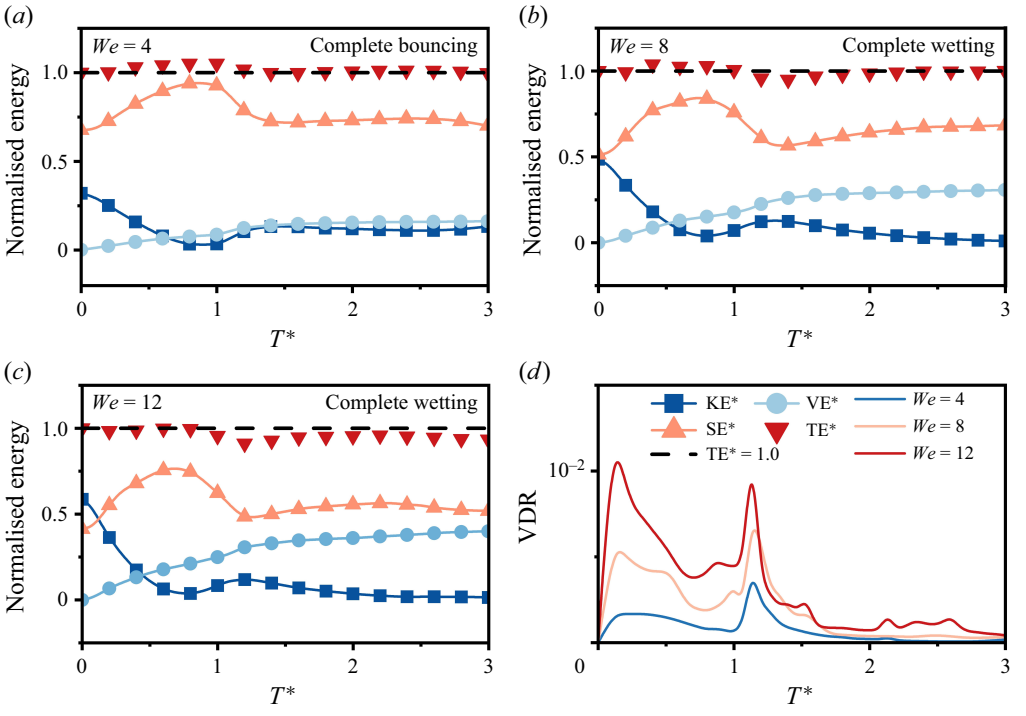


Figure 14. (*a–c*) Energy evolution of droplets at different *We,* and (*d*) transient evolution of the viscous dissipation rate (VDR) for $f = 0.6$ and $H^* = 0.17$.

and viscous dissipation increases. It is known that the evolution of SE and viscous dissipation is closely related to the spreading behaviour of the droplet, where a larger maximum spreading diameter results in a thinner liquid film, which implies higher SE and greater viscous dissipation. As shown in figure 6(*a*), at $We = 16$, there is no significant difference in the maximum spreading diameter across all cases. Therefore, no significant differences in the magnitude or evolution of the energy components are observed among the different micropillar geometries.

From the expression for SE, it can be seen that when a droplet impacts such a hybrid wettability surface, the total SE can be divided into three components, the gas–liquid interfacial energy ($SE_1 = \gamma_{lg} S_{lg}$), the hydrophobic interfacial energy ($SE_2 = -\gamma_{lg} \cos(\theta_p) S_{sl,p}$) and the hydrophilic interfacial energy ($SE_3 = -\gamma_{lg} \cos(\theta_b) S_{sl,b}$). We evaluated the average values of these components, as well as VE and KE, with all quantities normalised by the initial TE. As seen in figure 16(*a*), the proportion of viscous dissipation increases markedly with increasing *We*, consistent with the findings from figure 14. Notably, due to the increase in penetration depth and spreading diameter, SE_2 increases significantly with *We*. For Wenzel state droplets, the spreading area on the hydrophilic surface increases with increasing *We*, and thus, SE_3 also increases. It should be noted that this part of energy contribution is negative in magnitude, representing the energy input from capillary effects on the hydrophilic substrate. It should also be pointed out that, for the cases with the same impact *We*, although the proportions of VE and KE are similar across different θ_{eff} (as discussed in figure 15), both SE_1 and SE_3 decrease as θ_{eff} increases (as shown in figure 16*b*), indicating that less liquid is able to penetrate and wet the micropillars and the substrate, this result confirmed our dynamic analysis in § 3.1.

https://doi.org/10.1017/jfm.2026.11593 Published online by Cambridge University Press

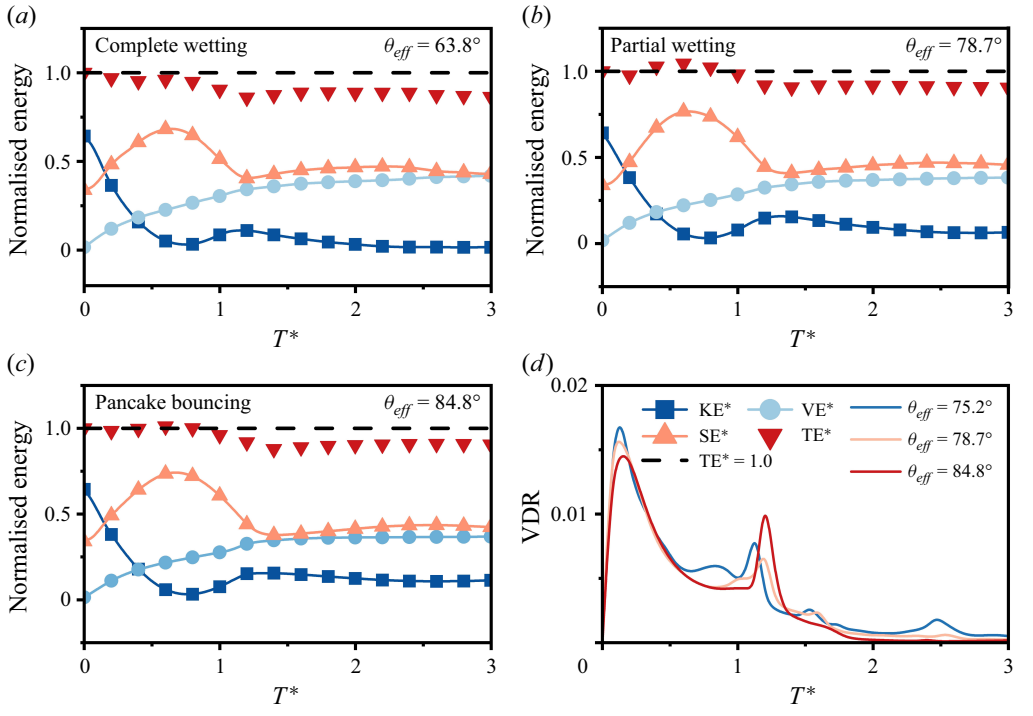


Figure 15. (*a–c*) Energy evolution of droplets at different effective contact angles (θ_{eff}), and (*d*) transient evolution of the VDR for $We = 16$

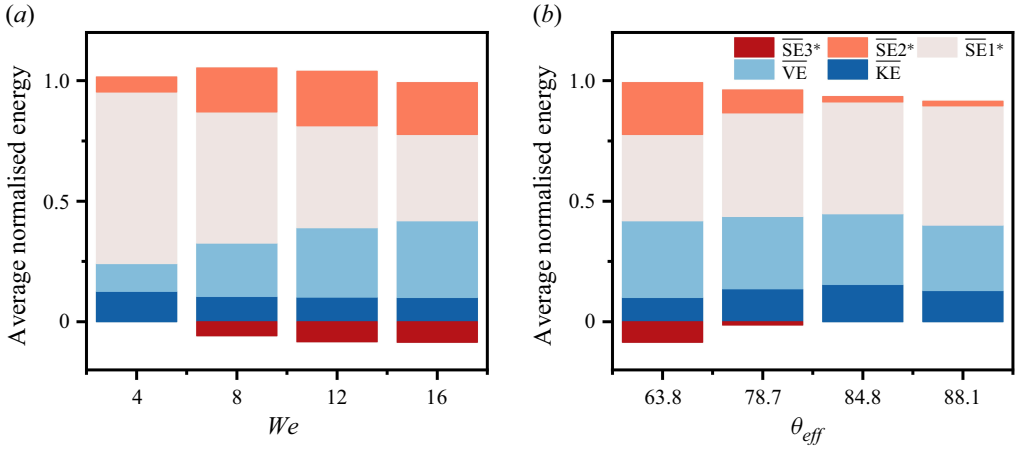


Figure 16. Time-averaged energy budget of the droplet during its evolution for cases with different (*a*) *We* and (*b*) effective contact angles (θ_{eff})

4. Conclusion

In this work we investigate droplet impact dynamics on a heterogeneous wettability surface composed of superhydrophobic micropillars on a hydrophilic substrate. A systematic parametric numerical study is conducted using an improved PF ULBM model to explore the effects of different surface geometries and impact conditions. Our

https://doi.org/10.1017/jfm.2026.11593 Published online by Cambridge University Press

study systematically addresses the following key problems for droplets impacting on heterogeneous wettability surfaces: (i) the bouncing and wetting morphologies and their underlying dynamic mechanisms, (ii) the analytical model for the droplet dynamic process and the criterion for determining the droplet's bouncing outcomes, (iii) the energy budget of the droplet during its evolution.

Firstly, our results revealed that droplets impacting heterogeneous wettability surfaces with varying pillar height (H^*) and opening fraction (f) can undergo either complete or partial penetration. For fully penetrated (Wenzel state) droplets, the liquid wets the hydrophilic substrate, resulting in partial wetting or complete wetting morphologies. In contrast, partially penetrated (Cassie state) droplets exhibit either complete bouncing or pancake bouncing morphologies, depending on the impact Weber number (We). Quantitative analysis of the spreading and penetration processes shows that at low We, limited penetration leads to complete rebound, with the maximum spreading factor β_{max} following classical scaling laws for droplet impact on flat superhydrophobic surfaces, and the solid–liquid contact time (t_c) approximating $t_c/\,t_\sigma \approx 2.2$. At higher We, increased penetration volume induces pancake bouncing with significantly reduced contact time, and β_{max} tends to a saturation value of 1.7. In wetting cases, strong adhesion to the hydrophilic substrate suppresses droplet rebound, and the maximum wetting area increases with increasing impact We.

Then, based on a force balance analysis, we propose a model (2.11) to describe the droplet penetration process in micropillar arrays, accounting for the effects of We, H^* and f. This model is further extended to predict the maximum penetration depth (2.15), providing a criterion for determining droplet morphologies based on the relationship between the maximum penetration depth (Δh^*_{max}) and pillar height (H^*). A transition diagram is constructed to delineate the complete rebound, pancake bouncing and wetting regions, with threshold boundaries derived from the proposed model. It is shown that droplets exhibit complete wetting for cases with $\Delta h^*_{max} - H^* \gg 0$ and partial wetting when $\Delta h^*_{max} - H^* \approx 0$. For Cassie state droplets with $\Delta h^*_{max} - H^* < 0$, the droplet undergoes complete rebound when $We < 12$ and pancake bouncing when $We > 12$.

Finally, we discuss the energy evolution during the droplet impact process. Our results show that for droplets impacting surfaces with the same geometry, viscous dissipation (VE) increases significantly with increasing We. In comparison, for cases with the same We, there is no significant difference in VE or KE among different surface geometries. By decomposing the SE contributions, we find that as We increases, the gas–liquid SE decreases, while the solid–liquid SE increases. In contrast, with increasing effective contact angle (θ_{eff}), the gas–liquid interfacial energy increases, whereas the solid–liquid interfacial energy decreases.

It should be emphasised that the force balance model proposed in this work (2.15) can be directly employed as a design criterion for heterogeneous wettability surfaces to achieve controllable droplet bouncing and wetting morphologies under different impacting parameters (as shown in figure 11). The physical insights developed in this study advance the fundamental understanding of droplet impact on heterogeneous wettability surfaces and establish a predictive framework for surface design. This framework holds significant potential for applications such as self-cleaning coatings, anti-icing surfaces and microfluidic devices, where controlled droplet behaviour is essential.

Acknowledgements. The authors gratefully acknowledge computational support provided by CoSeC, the Computational Science Centre for Research Communities, through UKCOMES.

Funding. This work was supported by the National Natural Science Foundation of China (grant nos 12502317 and 52506104), the National Key R&D Program of China (grant no. 2022YFF0503501), the UK Engineering

https://doi.org/10.1017/jfm.2026.11593 Published online by Cambridge University Press

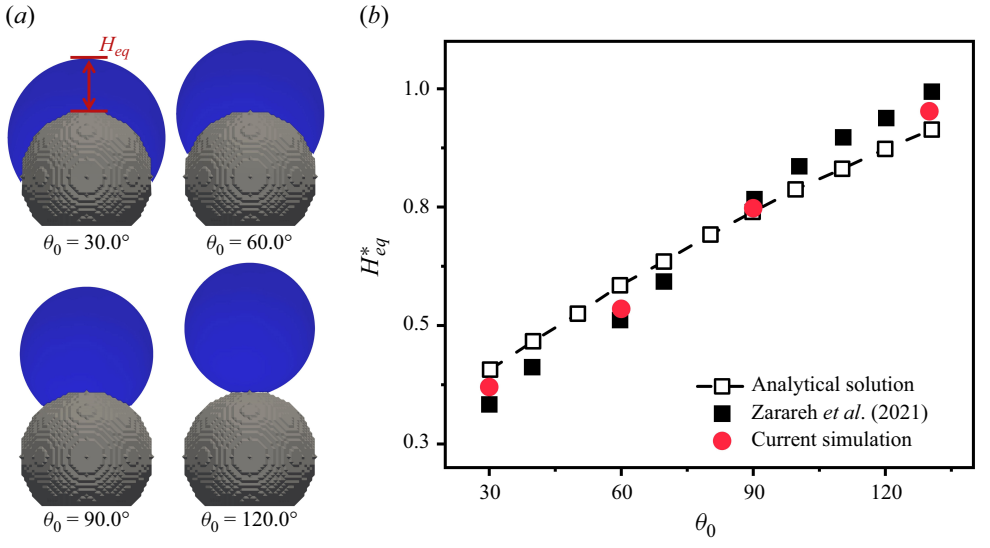


Figure 17. (*a*) Qualitative snapshots of steady-state droplets after wetting for different initial contact angles (θ_0). (*b*) Quantitative comparison of normalised equilibrium heights (H^*_{eq}) from our simulations with analytical prediction and previous numerical results.

and Physical Sciences Research Council through the project UK Consortium on Mesoscale Engineering Sciences (UKCOMES) (grant no. EP/X035875/1), and the National Key Laboratory of Spacecraft Thermal Control (grant no. NKLST-JJ-202401009).

Declaration of interests. The authors report no conflict of interest.

Appendix A. Validation of the contact angle model

We conducted a validation of the adopted contact angle model. In line with the validation cases reported by Zarareh *et al.* (2021), we simulated a droplet wetting a spherical solid surface with varying apparent contact angle (θ_0). In the initial state, both the droplet and the solid sphere have radius of 40 lattice units ($R_0 = R_s = 40$). The gas–liquid density ratio (ρ_l/ρ_g) is 1000, the droplet viscosity (μ_l) 0.1 and the surface tension (σ) 0.01 (all in lattice units). Figure 17(*a*) qualitatively displays the equilibrium heights (H_{eq}) of droplets after reaching a steady state for different wettabilities. Figure 17(*b*) quantitatively compares the normalised equilibrium heights ($H^*_{eq} = H_{eq}/R_0$) obtained from our simulations with the corresponding analytical prediction and the numerical results (Zarareh *et al.* 2021). It can be seen that our results are in excellent agreement with both previous numerical simulations and analytical prediction, demonstrating that our contact angle model can accurately simulate a wide range of wettability and complex surface geometries.

Appendix B. Grid independence test for droplet impact on micropillar surfaces

To verify the grid independence and interface thickness effects in the simulation of droplet impact on micropillar surfaces, we performed simulations for the case of $We = 7.9$ in figure 2 using various grid resolutions and interface thicknesses. In addition to the baseline grid parameters ($\mathrm{d}x = R_0/43$, $W_{int} = 5$), we further refined the grid resolution ($\mathrm{d}x = R_0/72$) and simultaneously reduced the interface thickness ($\mathrm{d}x = R_0/72$, $W_{int} = 3$). Figure 18(*a*) quantitatively presents the evolution of the dimensionless droplet radius.

https://doi.org/10.1017/jfm.2026.11593 Published online by Cambridge University Press

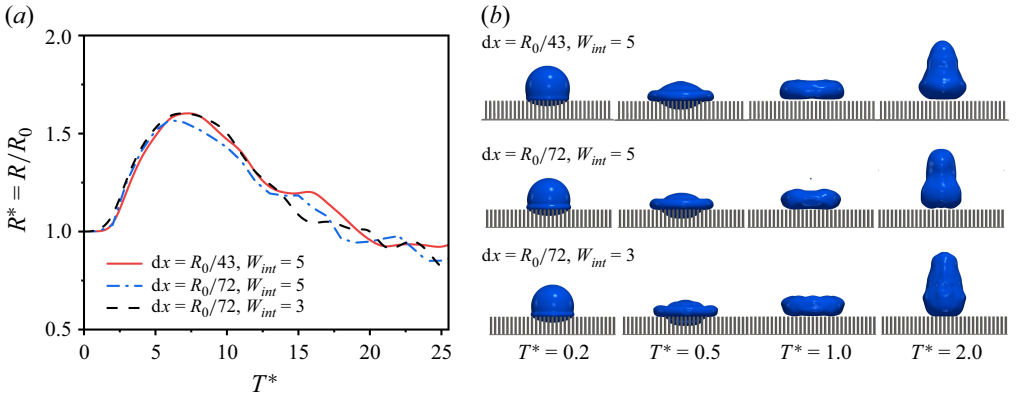


Figure 18. (*a*) Transient evolution and (*b*) qualitative snapshots of the normalised droplet radius for different grid resolutions and interface thicknesses.

It can be seen that the evolution is similar for all cases. However, due to the limitations imposed by the minimum grid resolution, the micropillar size may exhibit slight variations among the cases, which lead to small differences in the transient disturbance process. Figure 18(*b*) displays qualitative snapshots of the droplet. For all cases, the morphological evolution of the droplet is identical, especially for the key physical quantities of interest in this study, such as penetration depth at various time points and the rebound time. The presented results validate the grid independence of our simulations for droplet impact on micropillar surfaces with the current grid resolution.

References

Abe, R., 2020 Fabrication of $CH_3NH_3PbBr_3$-based perovskite single-crystal arrays by spin-coating method using hydrophobic patterned substrate. *Phys. Stat. Solidi (A)* **217** (3), 1–8.

Abolghasemibizaki, M., McMasters, R.L. & Mohammadi, R. 2018 Towards the shortest possible contact time: droplet impact on cylindrical superhydrophobic surfaces structured with macro-scale features. *J. Colloid Interface Sci.* **521**, 17–23.

Aidun, C.K. & Clausen, J.R. 2010 Lattice-Boltzmann method for complex flows. *Annu. Rev. Fluid Mech.* **42** (1), 439–472.

Barthlott, W. & Neinhuis, C. 1997 Purity of the sacred lotus, or escape from contamination in biological surfaces. *Planta* **202** (1), 1–8.

Bliznyuk, O., 2009 Scaling of anisotropic droplet shapes on chemically stripe-patterned surfaces. *Phys. Rev. E* **79** (4), 041601.

Bösch, F., Dorschner, B. & Karlin, I. 2018 Entropic multi-relaxation free-energy lattice Boltzmann model for two-phase flows. *EPL (Europhys. Lett.)* **122** (1), 14002.

Cao, L., 2009 Anti-icing superhydrophobic coatings. *Langmuir* **25** (21), 12444–12448.

Chen, L., 2011 A comparative study of droplet impact dynamics on a dual-scaled superhydrophobic surface and lotus leaf. *Appl. Surf. Sci.* **257** (21), 8857–8863.

Chen, Z. & Zhang, Z. 2020 Recent progress in beetle-inspired superhydrophilic-superhydrophobic micropatterned water-collection materials. *Water Sci. Technol.* **82** (2), 207–226.

Chiu, P.H. & Lin, Y.T. 2011 A conservative phase field method for solving incompressible two-phase flows. *J. Comput. Phys.* **230** (1), 185–204.

Dawson, J., 2023 Dynamics of droplets impacting on aerogel, liquid infused, and liquid-like solid surfaces. *ACS Appl. Mater. Interfaces* **15** (1), 2301–2312.

Delbos, A., Lorenceau, E. & Pitois, O. 2010 Forced impregnation of a capillary tube with drop impact. *J. Colloid Interface Sci.* **341** (1), 171–177.

Deng, T., 2009 Nonwetting of impinging droplets on textured surfaces. *Appl. Phys. Lett.* **94** (13), 2007–2010.

Ding, S., 2021 Droplet impact dynamics on single-pillar superhydrophobic surfaces. *Phys. Fluids* **33** (10), 102108.

https://doi.org/10.1017/jfm.2026.11593 Published online by Cambridge University Press

ERNEST, S., AUGUST, P.R.S.R. & STRUTT, J.W. 1879 On the capillary phenomena of jets. *P. R. Soc. Lond.* **29** (196–199), 71–97.
FEI, L., 2019 Modeling realistic multiphase flows using a non-orthogonal multiple-relaxation-time lattice Boltzmann method. *Phys. Fluids* **31** (4).
FEI, L., LUO, K.H. & LI, Q. 2018 Three-dimensional cascaded lattice Boltzmann method: improved implementation and consistent forcing scheme. *Phys. Rev. E* **97** (5), 053309.
FENG, W., UEDA, E. & LEVKIN, P.A. 2018 Droplet microarrays: from surface patterning to high-throughput applications. *Adv. Mater.* **30** (20), 1–17.
GAO, S.R., 2024 Experimental study on contact time of a water droplet impact under controlled surface temperature. *Phys. Fluids* **36** (3), 037133.
GAUTHIER, A., 2015 Water impacting on superhydrophobic macrotextures. *Nat. Commun.* **6**, 2–7.
GEIER, M., FAKHARI, A. & LEE, T. 2015 Conservative phase-field lattice Boltzmann model for interface tracking equation. *Phys. Rev. E* **91** (6), 1–11.
GIRARD, H.L., SOTO, D. & VARANASI, K.K. 2019 Waterbowls: reducing impacting droplet interactions by momentum redirection. *ACS Nano* **13** (7), 7729–7735.
GU, H., 2025 Leidenfrost effect on engineered surfaces. *Adv. Funct. Mater.* **36**, 1–19.
GUO, C., 2018 Droplet impact on cross-scale cylindrical superhydrophobic surfaces. *Appl. Phys. Lett.* **112** (26), 263702.
HE, B., 2024 Droplet splitting on chemically heterogeneous surface: a 3D lattice Boltzmann study. *Comput. Fluids* **270** (2023), 106149.
HOSSEINI, S.A. & KARLIN, I.V. 2023 Lattice Boltzmann for non-ideal fluids: fundamentals and practice. *Phys. Rep.* **1030**, 1–137.
HU, Z., 2022*a* Contact time of droplet impact on inclined ridged superhydrophobic surfaces. *Langmuir* **38** (4), 1540–1549.
HU, Z., 2023 Understanding and utilizing droplet impact on superhydrophobic surfaces: phenomena, mechanisms, regulations, applications, and beyond. *Adv. Mater.* **2310177**, 1–30.
HU, Z., CHU, F. & WU, X. 2022*b* Double-peak characteristic of droplet impact force on superhydrophobic surfaces. *Extreme Mech. Lett.* **52**, 101665.
HUANG, Y., 2013 A multi-stopband photonic-crystal microchip for high-performance metal-ion recognition based on fluorescent detection. *Angew. Chem. Intl Ed.* **52** (28), 7296–7299.
ILLIAS, S., 2021 Prediction of maximum spreading time of water droplet during impact onto hot surface beyond the Leidenfrost temperature. *Case Stud. Thermal Engng* **28** (September), 101396.
JACQMIN, D. 2000 Contact-line dynamics of a diffuse fluid interface. *J. Fluid Mech.* **402**, 57–88.
JAIN, S.S. 2022 Accurate conservative phase-field method for simulation of two-phase flows. *J. Comput. Phys.* **469**, 111529.
JANSEN, H.P., 2012 Simulating anisotropic droplet shapes on chemically striped patterned surfaces. *Langmuir* **28** (1), 499–505.
JOSSERAND, C. & THORODDSEN, S.T. 2016 Drop impact on a solid surface. *Annu. Rev. Fluid Mech.* **48**, 365–391.
JOSYULA, T., 2024 Fundamentals and applications of surface wetting. *Langmuir* **40** (16), 8293–8326.
KUMAR, A., 2018 Effect of geometrical parameters on rebound of impacting droplets on leaky superhydrophobic meshes. *Soft Matt.* **14** (9), 1571–1580.
KUSUMAATMAJA, H. & YEOMANS, J.M. 2007 Modeling contact angle hysteresis on chemically patterned and superhydrophobic surfaces. *Langmuir* **23** (11), 6019–6032.
LAFUMA, A. & QUÉRÉ, D. 2003 Superhydrophobic states. *Nat. Mater.* **2** (7), 457–460.
LEE, S.H., 2017 A numerical study on the separation of droplet on the heterogeneous surface. *Comput. Fluids* **152**, 231–247.
LEITE, Á.J., 2017 Screening of nanocomposite scaffolds arrays using superhydrophobic-wettable micropatterns. *Adv. Funct. Mater.* **27** (28), 1–12.
LENG, M., 2018 All-inorganic bismuth-based perovskite quantum dots with bright blue photoluminescence and excellent stability. *Adv. Funct. Mater.* **28** (1), 1–11.
LENZ, P. & LIPOWSKY, R. 1998 Morphological transitions of wetting layers on structured surfaces. *Phys. Rev. Lett.* **80** (9), 1920–1923.
LI, H., 2015 Splitting a droplet for femtoliter liquid patterns and single cell isolation. *ACS Appl. Mater. Interfaces* **7** (17), 9060–9065.
LI, H., FANG, W., 2020*a* Droplet precise self-splitting on patterned adhesive surfaces for simultaneous multidetection. *Angew. Chem. Intl Edn* **59** (26), 10535–10539.
LI, H., LI, A., 2020*b* Heterogeneous wettability surfaces: principle, construction, and applications. *Small Struct.* **1** (2), 1–13.

https://doi.org/10.1017/jfm.2026.11593 Published online by Cambridge University Press

LI, Q., 2016 Lattice Boltzmann methods for multiphase flow and phase-change heat transfer. *Prog. Energy Combust.* **52** (0), 62–105.
LI, Q., LUO, K.H. & LI, X.J. 2012 Forcing scheme in pseudopotential lattice Boltzmann model for multiphase flows. *Phys. Rev. E* **86** (1), 016709.
LIANG, G. & MUDAWAR, I. 2017*a* Review of drop impact on heated walls. *Intl J. Heat Mass Transfer* **106**, 103–126.
LIANG, G. & MUDAWAR, I. 2017*b* Review of spray cooling – Part 1: single-phase and nucleate boiling regimes, and critical heat flux. *Intl J. Heat Mass Transfer* **115**, 1174–1205.
LIANG, H., 2023 Lattice Boltzmann method for interface capturing. *Phys. Rev. E* **107** (2), 025302.
LIU, Y., MOEVIUS, L., XU, X., QIAN, T., YEOMANS, J.M. & WANG, Z. 2014 Pancake bouncing on superhydrophobic surfaces. *Nat. Phys.* **10** (7), 515–519.
LIU, Y., ANDREW, M., LI, J., YEOMANS, J.M. & WANG, Z. 2015 Symmetry breaking in drop bouncing on curved surfaces. *Nat. Commun.* **6**, 10034.
LOHSE, D. 2021 Fundamental fluid dynamics challenges in inkjet printing. *Annu. Rev. Fluid Mech.* **54**, 349–382.
LUO, D., ZHANG, J., ZENG, X., ZHANG, M., ZENG, X. & ZHOU, C. 2023 Fabrication and target applications of hydrophilic-hydrophobic composite wettability surfaces based on surface wettability gradient and Laplace pressure gradient regulation. *Appl. Mater. Today* **35** (September), 101957.
LUO, K.H., FEI, L. & WANG, G. 2021 A unified lattice Boltzmann model and application to multiphase flows. *Phil. Trans. R. Soc. A* **379** (2208), 20200397.
MAJHY, B., SINGH, V.P. & SEN, A.K. 2020 Understanding wetting dynamics and stability of aqueous droplet over superhydrophilic spot surrounded by superhydrophobic surface. *J. Colloid Interface Sci.* **565**, 582–591.
MAZLOOMI, M., CHIKATAMARLA, A., SS, & KARLIN, I.V. 2015 Entropic lattice Boltzmann method for multiphase flows: fluid-solid interfaces. *Phys. Rev. E* **92** (2), 1–10.
MAZLOOMI MOQADDAM, A., CHIKATAMARLA, S.S. & KARLIN, I.V. 2017 Drops bouncing off macro-textured superhydrophobic surfaces. *J. Fluid Mech.* **824**, 866–885.
MILNE, A.J.B.B., AMIRFAZLI, A. & BAXTER, C. 2012 The Cassie equation: how it is meant to be used. *Adv. Colloid Interface Sci.* **170** (1–2), 48–55.
MOEVIUS, L., LIU, Y., WANG, Z. & YEOMANS, J.M. 2014 Pancake bouncing: simulations and theory and experimental verification. *Langmuir* **30** (43), 13021–13032.
MURAKAMI, D., JINNAI, H. & TAKAHARA, A. 2014 Wetting transition from the Cassie–Baxter state to the Wenzel state on textured polymer surfaces. *Langmuir* **30** (8), 2061–2067.
PARKER, A.R. & LAWRENCE, C.R. 2001 Water capture by a desert beetle. *Nature* **414** (6859), 33–34.
PHILIPPI, J., LAGRÉE, P.-Y. & ANTKOWIAK, A. 2016 Drop impact on a solid surface: short-time self-similarity. *J. Fluid Mech.* **795**, 96–135.
QUÉRÉ, D. 2002 Fakir droplets. *Nat. Mater.* **1** (1), 14–15.
RAYLEIGH, L. 1879 On the capillary phenomena of jets. *Proc. R. Soc. Lond.* 29, 71–97.
REYSSAT, M. & QUÉRÉ, D. 2009 Contact angle hysteresis generated by strong dilute defects. *J. Phys. Chem. B* **113** (12), 3906–3909.
RIBOUX, G. & GORDILLO, J.M. 2014 Experiments of drops impacting a smooth solid surface: a model of the critical impact speed for drop splashing. *Phys. Rev. Lett.* **113** (2), 1–5.
RICHARD, D., CLANET, C. & QUÉRÉ, D. 2002*a* Contact time of a bouncing drop. *Nature* **417** (6891), 811–811.
RICHARD, D., CLANET, C. & QUÉRÉ, D. 2002*b* Surface phenomena: contact time of a bouncing drop. *Nature* **417** (6891), 811.
RIOBOO, R., TROPEA, C. & MARENGO, M. 2001 Outcomes from a drop impact on solid surfaces. *Atomiz. Spray* **11** (2), 12–165.
ROTHSTEIN, J.P. 2010 Slip on superhydrophobic surfaces. *Annu. Rev. Fluid Mech.* **42** (June), 89–109.
SHEN, Y., LIU, S., ZHU, C., TAO, J., CHEN, Z., TAO, H., PAN, L., WANG, G. & WANG, T. 2017 Bouncing dynamics of impact droplets on the convex superhydrophobic surfaces. *Appl. Phys. Lett.* **110** (22), 221601.
SONG, J., GAO, M., ZHAO, C., LU, Y., HUANG, L., LIU, X., CARMALT, C.J., DENG, X. & PARKIN, I.P. 2017 Large-area fabrication of droplet pancake bouncing surface and control of bouncing state. *ACS Nano* **11** (9), 9259–9267.
STRUTT, J.W. 2011 On the capillary phenomena of jets. In *Scientific Papers*. pp. 377–401. JSTOR.
TAO, R., LIANG, G., DOU, B., WU, J., LI, B. & HAO, C. 2022 Oblique pancake bouncing. *Cell Rep. Phys. Sci.* **3** (1), 100721.
UNVERDI, S.O. & TRYGGVASON, G. 1992 A front-tracking method for viscous, incompressible, multi-fluid flows. *J. Comput. Phys.* **100** (1), 25–37.

https://doi.org/10.1017/jfm.2026.11593 Published online by Cambridge University Press

WANG, F., WU, Y. & NESTLER, B. 2023*a* Wetting effect on patterned substrates. *Adv. Mater.* **35** (25), e2210745.

WANG, G., *et al.* 2023*b* A three-dimensional non-orthogonal multiple-relaxation-time phase-field lattice Boltzmann model for multiphase flows at large density ratios and high Reynolds numbers. *Intl J. Multiphase Flow* **168**, 104582.

WANG, G., LEI, T., YANG, J., FEI, L., CHEN, J. & LUO, K.H. 2024 Lattice Boltzmann modelling and study of droplet equatorial streaming in an electric field. *J. Fluid Mech.* **988**, 1–37.

WANG, G., SOHANI, S.M., YANG, J., LEI, T., CHEN, J., HE, R. & LUO, K.H. 2025 Study of oblique impingement of water droplets on superhydrophobic surfaces patterned with micropillars: a lattice Boltzmann approach. *Appl. Therm. Engng* **262** (August 2024), 125231.

WANG, G., FEI, L. & LUO, K.H. 2022 Unified lattice Boltzmann method with improved schemes for multiphase flow simulation: application to droplet dynamics under realistic conditions. *Phys. Rev. E* **105** (4), 045314.

WANG, X., XU, B., GUO, S., ZHAO, Y. & CHEN, Z. 2023*c* Droplet impacting dynamics: recent progress and future aspects. *Adv. Colloid Interface Sci.* **317** (May), 102919.

WANG, Y., ZHAO, J., ZHANG, D., JIAN, M., LIU, H. & ZHANG, X. 2019 Droplet sliding: the numerical observation of multiple contact angle hysteresis. *Langmuir* **35** (30), 9970–9978.

WÖHRWAG, M., SEMPREBON, C., MAZLOOMI MOQADDAM, A., KARLIN, I. & KUSUMAATMAJA, H. 2018 Ternary free-energy entropic lattice Boltzmann model with a high density ratio. *Phys. Rev. Lett.* **120** (23), 234501.

WÖRNER, M. 2023 Maximum spreading of an impacting drop. *Intl J. Multiphase Flow* **167** (May), 104528.

WORTHINGTON, A.M. 1908 *A Study of Splashes*. Longmans, Green, and Company.

WU, Y., WANG, F., SELZER, M. & NESTLER, B. 2019 Investigation of equilibrium droplet shapes on chemically striped patterned surfaces using phase-field method. *Langmuir* **35** (25), 8500–8516.

WU, Y., WANG, F., MA, S., SELZER, M. & NESTLER, B. 2020 How do chemical patterns affect equilibrium droplet shapes? *Soft Matt.* **16** (26), 6115–6127.

WU, Y., WANG, F., MA, S., SELZER, M. & NESTLER, B. 2022 Equilibrium droplet shapes on chemically patterned surfaces: theoretical calculation, phase-field simulation, and experiments. *J. Colloid Interface Sci.* **606**, 1077–1086.

XIA, L., YANG, Z., CHEN, F., LIU, T., TIAN, Y. & ZHANG, D. 2024 Droplet impacting on pillared hydrophobic surfaces with different solid fractions. *J. Colloid Interface Sci.* **658** (October 2023), 61–73.

YAN, Y.Y., GAO, N. & BARTHLOTT, W. 2011 Mimicking natural superhydrophobic surfaces and grasping the wetting process: a review on recent progress in preparing superhydrophobic surfaces. *Adv. Colloid Interface Sci.* **169** (2), 80–105.

YANG, J., XU, Q., KOU, X., WANG, G., LEI, T., WANG, Y., LI, X. & LUO, K.H. 2024 Three-dimensional pore-scale study of methane hydrate dissociation mechanisms based on micro-CT images. *The Innovation Energy* **1** (1), 100015.

YANG, Y., XU, L.-P., ZHANG, X. & WANG, S. 2020 Bioinspired wettable-nonwettable micropatterns for emerging applications. *J. Mater. Chem. B* **8** (36), 8101–8115.

YARIN, A.L. 2006 Drop impact dynamics: splashing, spreading, receding, bouncing. *Annu. Rev. Fluid Mech.* **38**, 159–192.

YOSHIMITSU, Z., NAKAJIMA, A., WATANABE, T. & HASHIMOTO, K. 2002 Effects of surface structure on the hydrophobicity and sliding behavior of water droplets. *Langmuir* **18** (15), 5818–5822.

YOUNG, T. 1805 An essay on the cohesion of fluids. *Phil. Trans. R. Soc. Lond.* **95**, 65–87.

YU, X., ZHANG, Y., HU, R. & LUO, X. 2021 Water droplet bouncing dynamics. *Nano Energy* **81** (November 2020), 105647.

YUE, P., ZHOU, C. & FENG, J.J. 2010 Sharp-interface limit of the Cahn-Hilliard model for moving contact lines. *J. Fluid Mech.* **645**, 279–294.

ZARAREH, A., KHAJEPOR, S., BURNSIDE, S.B. & CHEN, B. 2021 Improving the staircase approximation for wettability implementation of phase-field model: Part 1 – Static contact angle. *Comput. Math. Appl.* **98**, 218–238.

ZHANG, B., 2022 Impact forces of water drops falling on superhydrophobic surfaces. *Phys. Rev. Lett.* **129** (10), 104501.

ZHAO, Z., LI, H., LIU, Q., LI, A., XUE, L., YUAN, R., YU, X., LI, R., DENG, X. & SONG, Y. 2023 Regulating droplet impact symmetry by surface engineering. *Droplet* **2** (2), e52.

ZHU, H., HUANG, Y., LOU, X. & XIA, F. 2019 Beetle-inspired wettable materials: from fabrications to applications. *Materials Today Nano* **6**, 100034.

https://doi.org/10.1017/jfm.2026.11593 Published online by Cambridge University Press